Journal of Sound and Vibration 562 (2023) 117821

Contents lists available at ScienceDirect

Journal of Sound and Vibration

journal homepage: www.elsevier.com/locate/jsvi

Nonlinearity enhanced wave bandgaps in metamaterial honeycombs embedding spider web-like resonators

Yichang Shen *, Walter Lacarbonara

Department of Structural and Geotechnical Engineering, SAPIENZA University of Rome, Rome, 00184, Italy

ARTICLE INFO

Keywords:
Metamaterial honeycomb
Dispersion properties
Method of multiple scales
Nonlinear wave propagation
Nonlinear resonators

ABSTRACT

Wave propagation in metamaterial honeycombs endowed with periodically distributed nonlinear resonators is addressed. The linear and nonlinear dispersion properties of the metamaterial are investigated. The nonlinear wave propagation equations obtained via a projection method and the Floquet–Bloch theorem are attacked by the method of multiple scales to obtain in closed form the nonlinear manifolds parametrized by the amplitudes, the frequency, and the wave numbers. The effects of the nonlinearity on the frequency bandgaps are thoroughly investigated and the optimization problem of the resonators nonlinearity towards increased bandgap size is tackled to provide a significant practical framework for the design of nonlinear metamaterials.

1. Introduction

Periodic structures are attracting a great deal of attention thanks to their potential for suppressing or attenuating the propagation of elastic waves [1,2]. The possibility of manipulating the band gaps [3,4] allows to exploit the advantageous characteristics of these periodically architected materials for vibration or sound attenuation purposes [5]. The formation of a band gap is one of the most attractive features and includes both Bragg scattering and local resonance gaps phenomena. The former is achieved when destructive interferences are created by the geometric properties of such lattices, the latter is a locally resonant (LR) mechanism meant to create prevalently low-frequency band gaps [6]. While Bragg scattering occurs if the period of the structure is of the same order as the wavelength of the band gap frequencies, resulting into a substantial difficulty of forming low-frequency band gaps, periodic LR structures, realized as arrays of resonators attached to a hosting structure, are independent from the size of the unit cell and can achieve vibration suppression across a bandwidth which is two order-of-magnitude lower than that given by the Bragg limit [7].

The possibility of creating and optimizing targeted flexural wave band gaps in 2D locally resonant periodic structures thanks to the resonators nonlinearity is one of the main goals of the present work. Initial studies addressing 2D LR periodic structures with linear resonators can be found in [8–19]. Lattice structures and resonator architectures in different shapes have been proposed for wave propagation control [20–24]. For example, a periodic and aperiodic composite metamaterial design was proposed and experimentally investigated in [25]. The metamaterial LR system, mimicking the idea of locally resonant sonic crystals discussed in [26], consists of a polymeric casing which embeds in its skeleton spherical and cylindrical steel masses; the rigid steel masses enhance the effective mass density, and thus allow the resonant system to generate wide, low-frequency band gaps distributed over a broad frequency range with a bandwidth gap to mid-gap ratio of 181%.

The background of the present work is represented by the study carried out by the same authors on a cellular metamaterial beam with multi-resonators possessing nonlinear (cubic) restoring forces [27]. The formation of multiple band gaps with various bandwidths was demonstrated together with the significant enlargement of the band gaps triggered by the nonlinear resonators

* Corresponding author.
E-mail addresses: shenyichang93@163.com (Y. Shen), walter.lacarbonara@uniroma1.it (W. Lacarbonara).

https://doi.org/10.1016/j.jsv.2023.117821
Received 5 December 2022; Received in revised form 8 May 2023; Accepted 24 May 2023
Available online 29 May 2023

forces giving rise to nonlinear resonances. Here, we provide design conditions to maximally leverage on the beneficial effects of the resonators softening/hardening nonlinearity towards the enhancement of the stop bands size in the metamaterial honeycomb making use of the asymptotic solutions [28]. The effects of dissipation in a 1D hosting medium made of linear springs with a periodic distribution of nonlinear, hysteretically damped resonators were previously tackled using an extended Hamiltonian approach and Lie series [29].

Among the analytical methods available in the literature, the well-known Plane Wave Expansion (PWE) method [30], also called $\omega(\mathbf{K})$, is one of the effective approaches to tackle wave propagation in periodic resonant systems. In [31], by taking into account the classical Kirchhoff–Love plate theory, the influence of the periodic array of one-degree-of-freedom (1-dof) resonators embedded in square and hexagonal lattice structures was studied employing the PWE method. The single-dof resonator system is characterized by one complete band gap at low frequencies, whereas by introducing multi-frequency resonators (i.e., several resonators per unit cell), it is possible to increase the number of band gaps of the LR structures [32]. In a recent work [33], a locally resonant isotropic plate, hosting multiple arrays of multi-dof spring–mass resonators, was investigated. Interesting results regarding the band gap properties, including the location, the bandwidth, and the attenuation strength of the band gaps, as well as the effect of damping in the resonators were analyzed.

The method of multiple scales [34] is a classical tool for asymptotic analysis of weakly nonlinear dynamical problems and is widely employed for the study of metamaterials and lattices. In [35], the authors estimated the amplitude-dependent dispersion relationships of a configurable one-dimensional periodic chain with stiffness nonlinearity by making use of the method of multiple scales. Then, two-dimensional weakly nonlinear lattices were investigated asymptotically in [36], where a special focus was put on the invariant waveforms and stability analysis. Again, by employing the method of multiple scales, Bukhari and Barry [37] investigated a nonlinear metamaterial consisting of a nonlinear chain with multiple nonlinear local resonators, obtaining the relationship between the space–time domain and nonlinear dispersion properties. The asymptotic method was also employed in the context of several other studies dealing, for example, with nonlinear lattices undergoing internal resonances (see, e.g., [38,39]), exhibiting nonlinear monoatomic chains (see, e.g., [40–42]).

A key role in studies dealing with 2D cellular structures hosting resonators is also played by the homogenization approach implemented to obtain equivalent continuum plate-like models. The model proposed by [43] is one of the popular homogenization approaches for honeycomb-shaped 2D cellular structures yielding analytical expressions of the equivalent continuum elastic coefficients. This approach assumes the periodicity of the honeycomb cells treated as a beam network system in which each cell wall segment is modeled as a beam. A good agreement between numerical and experimental investigations was shown. More recent studies [44] improved the honeycomb homogenization model presented in [43] by also considering the effect of the stress in the cell vertices which becomes more relevant for increasing values of the relative density. The homogenization approach was further extended in [45] to cover a sufficiently general class of honeycomb periodic cells with different hexagonal shapes.

In this paper, we first discuss the modeling approach yielding the equations governing wave propagation. Then the nonlinear dispersion relationships are obtained via the method of multiple scales in order to study the nonlinear stop band optimization problem. The optimization approach yields a design chart through which the optimal nonlinearity of the resonators can be selected for a given metamaterial with a targeted frequency range.

2. Problem formulation and metamaterial modeling

Fig. 1 shows the reference configuration of the infinitely long, equivalent orthotropic plate whose reference planes lies in the $\mathbf{e}_1 - \mathbf{e}_2$ coordinate plane of the fixed frame while the equivalent spider-web-like resonators positions are ruled by the lattice vectors $(\mathbf{a}_1, \mathbf{a}_2)$. Each multi-frequency resonator should be meant as the multi-mass–spring system resulting from the multi-dof modal reduction of the infinite-dimensional resonator (i.e., the spider webs with a central mass, here represented in the figure, for the sake of graphical clarity, by a single mass–spring system instead of a set of mass–spring systems). The modal reduction is performed via the Galerkin projection method employing a number of mode shapes of the distributed-parameter resonators. Therefore, each resonator is represented by equivalent modal masses and modal springs positioned at the lattice points $\mathbf{x}_j = m\mathbf{a}_1 + n\mathbf{a}_2$, with m and n being integers, $\mathbf{a}_1 = (a_{11}, a_{12}) = (a, 0)$ and $\mathbf{a}_2 = (a_{21}, a_{22}) = \frac{a}{2}(1, \sqrt{3})$ being the direct lattice vectors and a is the lattice parameter.

The equivalent orthotropic model of the honeycomb derived from the homogenization originally proposed in [43] and enhanced in [44] employs the equivalent elastic moduli [46] expressed as $(E^\star_\alpha, G^\star_{\alpha\beta}, \nu^\star_{\alpha\beta})$, for $\alpha, \beta = 1, 2, 3$, and mass density ρ^* of the equivalent orthotropic material.

The adopted plate theory (see [47]) with the elastic constants of the equivalent, homogenized orthotropic material describes the motion of the honeycomb with the attached resonators. The equations of motion for the orthotropic plate-resonator coupled system are

$$\rho^\star h \frac{\partial^2 w(\mathbf{x},t)}{\partial t^2} + \left[D^*_{11} \frac{\partial^4 w(\mathbf{x},t)}{\partial x_1^4} + (2D^*_{12} + 4D^*_{66}) \frac{\partial^4 w(\mathbf{x},t)}{\partial x_1^2 \partial x_2^2} + D^*_{22} \frac{\partial^4 w(\mathbf{x},t)}{\partial x_2^4} \right] + \\ + \sum_{i,j} M_{ij} \left[\ddot{w}(\mathbf{x},t) + \ddot{z}_{ij}(t) \right] \delta(\mathbf{x} - \mathbf{x}_j) = 0, \tag{1}$$

$$M_{ij} \left[\ddot{w}(\mathbf{x}_j,t) + \ddot{z}_{ij}(t) \right] + K_{ij} z_{ij}(t) + N^{(3)}_{ij} z^3_{ij}(t) = 0, \quad i = 1, \dots, N, \quad j = -\infty, \infty \tag{2}$$

where $\mathbf{x} = x_1\mathbf{e}_1 + x_2\mathbf{e}_2$ is the position vector for a material point of the plate mid-surface, t is time, $w(\mathbf{x})$ is the displacement of the plate at $\mathbf{x}$, z_{ij} is the displacement of the jth resonator placed at $\mathbf{x}_j$ vibrating in its ith mode, N is the number of retained resonators

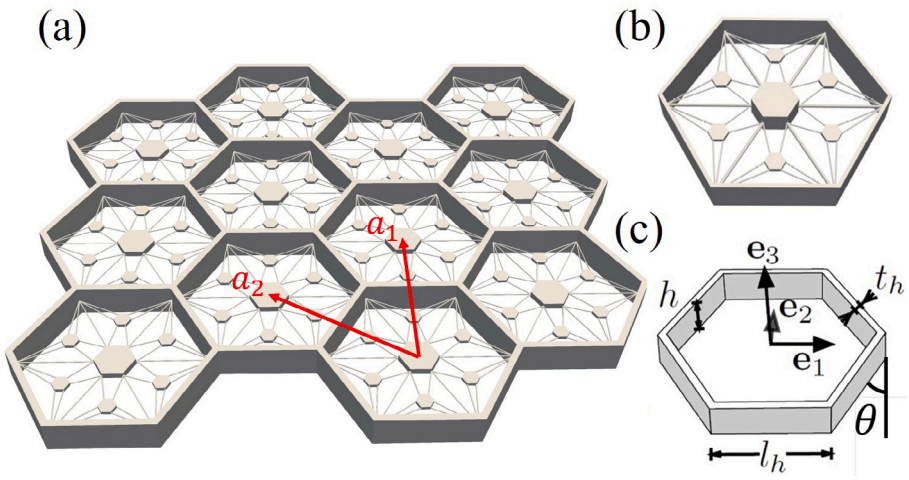

Fig. 1. (a) Schematic view of the orthotropic plate models with the periodically distributed spider-web resonators (shown in (b)). (c) The hexagonal cell geometry with height h, side length l_h, thickness t_h, and angle θ. The hexagonal lattice vectors are denoted by $(\mathbf{a}_1, \mathbf{a}_2)$ and the fixed frame by $(\mathbf{e}_1, \mathbf{e}_2, \mathbf{e}_3)$.

modes, h is the thickness of the honeycomb plate, while $D^{\star}_{rs}$ are the plate bending stiffness coefficients, and $\rho^{\star}$ is the density of the equivalent plate whose expressions are reported in Appendix A; K_{ij}, M_{ij} and $\tilde{N}^{(3)}_{ij}$ are the ith modal stiffness, modal mass, and nonlinearity of the jth resonator, $\delta(\mathbf{x}-\mathbf{x}_j)$ is the 2D Dirac-delta function introduced to localize the inertia force of the jth resonator at its reference position.

By employing the Floquet–Bloch Theorem which states that the solutions of the corresponding linear periodic resonators-plate system are quasi-periodic in space with the fundamental periodicity provided by the lattice period, the solution is sought as $w(x_1, x_2, t) = w_0(t)e^{i(k_1 x_1 + k_2 x_2)}$ and $z_{ij}(x_{1j}, x_{2j}, t) = z_{i0}(t)e^{i(k_1 x_{1j} + k_2 x_{2j})}$ where $w_0(t) = w(0,0,t)$ and $z_{i0}(t) := z_{i0}(0,0,t)$ denote the plate deflection and the resonator relative motion at the origin of the fixed frame. Upon substitution of the assumed solution into (1), one obtains

$$\begin{aligned}
&\left[\rho^{\star}h\ddot{w}_0(t) + [k_1^4 D^*_{11} + k_1^2 k_2^2(2D^*_{12} + 4D^*_{66}) + k_2^4 D^*_{22}]w_0(t)\right] e^{i(k_1 x_1 + k_2 x_2)} \\
&\qquad + \sum_{i,j} M_{ij}\left[\ddot{w}_0(t) + \ddot{z}_{i0}(t)\right] e^{i(k_1 x_1 + k_2 x_2)}\delta(x_1 - x_{1j})\delta(x_2 - x_{2j}) = 0, \\
&\qquad M_{ij}\left[\ddot{w}_0(t) + \ddot{z}_{i0}(t)\right] + K_{ij} z_{i0}(t) + N^{(3)}_{ij} z^3_{i0}(t) = 0.
\end{aligned} \tag{3}$$

Given the periodicity of the solution, the plate equation of motion is projected onto the unit cell domain Ω_x (i.e., the periodic ally repeated lattice unit) to yield

$$\begin{aligned}
&\int_{\Omega_x}\left[\rho^{\star}h\ddot{w}_0(t) + (k_1^4 D^*_{11} + k_1^2 k_2^2(2D^*_{12} + 4D^*_{66}) + k_2^4 D^*_{22})w_0(t)\right] e^{i(k_1 x_1 + k_2 x_2)} dx_1 dx_2 \\
&\quad + \int_{\Omega_x}\left\{\sum_{ij} M_{ij}\left[\ddot{w}_0(t) + \ddot{z}_{i0}(t)\right] e^{i(k_1 x_1 + k_2 x_2)}\delta(x_1 - x_{1j})\delta(x_2 - x_{2j})\right\} dx_1 dx_2 = 0, \\
&\quad M_{ij}\left[\ddot{w}_0(t) + \ddot{z}_{i0}(t)\right] + K_{ij} z_{i0}(t) + N^{(3)}_{ij} z^3_{i0}(t) = 0.
\end{aligned} \tag{4}$$

A schematic view of the honeycomb plate is shown in Fig. 2(a), with the corresponding cell domain mapping Ω_x in Fig. 2(b). The idea is to transform the parallelogram region Ω_x into the rectangular domain Ω_y (see Fig. 2(c)) for computational convenience. To this end, the transformation matrix $\mathbf{J}$ is introduced according to

$$\begin{Bmatrix} y_1 \\ y_2 \end{Bmatrix} = \begin{bmatrix} J_{11} & J_{12} \\ J_{21} & J_{22} \end{bmatrix} \begin{Bmatrix} x_1 \\ x_2 \end{Bmatrix}, \tag{5}$$

where (x_1, x_2) are the coordinates of P or Q shown in Fig. 2(b), and (y_1, y_2) are the corresponding coordinates in Fig. 2(c). The mapping $\mathbf{J}$ can thus be solved as follows

$$\mathbf{J} = \begin{bmatrix} 1 & -1/\sqrt{3} \\ 0 & 2/\sqrt{3} \end{bmatrix}. \tag{6}$$

Therefore, one can make use of the coordinate transformation to obtain the integral of any term of the equation of motion (here denoted by function $f(\mathbf{x})$) over Ω_x

$$\int_{\Omega_x} f(\mathbf{x}) dA_x = \int_{\Omega_y} f(\mathbf{y}) \det(\mathbf{J}^{-1}) dA_y. \tag{7}$$

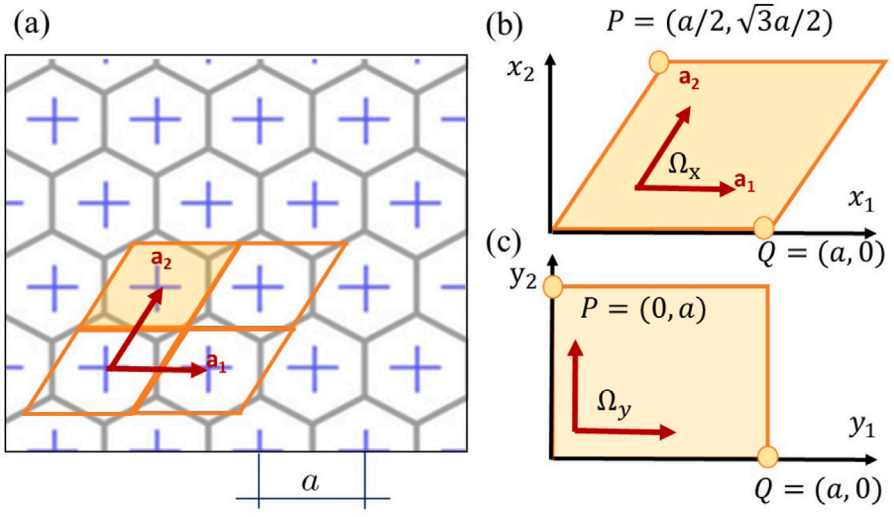

Fig. 2. (a) Schematic view of the cell mapping domain, (b) Ω_x before transformation, (c) Ω_y after transformation.

Hence,

$$\int_{\Omega_x} f(x_1,x_2)dx_1dx_2 = \int_{-a/2}^{a/2}\int_{-a/2}^{a/2} f(y_1,y_2)\det(\mathbf{J}^{-1})dy_1dy_2 = \int_{-a/2}^{a/2}\int_{-a/2}^{a/2} f(y_1,y_2)\frac{\sqrt{3}}{2}dy_1dy_2 \tag{8}$$

Finally, $\mathbf{x} = \mathbf{J}^{-1}\mathbf{y}$ yields the following transformation:

$$x_1 = y_1 + \frac{y_2}{2}, \quad x_2 = \frac{\sqrt{3}y_2}{2}, \tag{9}$$

which shows the parametric relation of the cell domain coordinates before and after transformation.

Upon introducing the coordinates transformation, by setting:

$$\begin{aligned} A(k_1,k_2) &:= \int_{\Omega_x} e^{i(k_1x_1+k_2x_2)}dx_1dx_2 = \int_{-a/2}^{a/2}\int_{-a/2}^{a/2} e^{i(k_1(y_1+y_2/2)+k_2(\sqrt{3}y_2/2))}\frac{\sqrt{3}}{2}dy_1dy_2 \\ &= \frac{4\sqrt{3}\sin\left(\frac{ak_1}{2}\right)\sin\left(\frac{1}{4}a\left(k_1+\sqrt{3}k_2\right)\right)}{k_1\left(k_1+\sqrt{3}k_2\right)} \end{aligned} \tag{10}$$

and upon defining the following nondimensional variables and parameters:

$$\begin{aligned} &\tilde{x}_1 = \frac{x_1}{a},\ \tilde{x}_2 = \frac{x_2}{a},\ \tilde{t} = \omega_0 t,\ \omega_0 = \sqrt{\frac{D_{11}^*}{\rho^* h a^4}},\ \tilde{w} = \frac{w}{a},\ \tilde{z}_{ij} = \frac{z_{ij}}{a},\ \tilde{\mathbf{x}}_j = \frac{\mathbf{x}_j}{a},\ \tilde{\mathbf{k}} = \mathbf{k}a, \\ &\tilde{K}_{ij} = \frac{K_{ij}a^2}{D_{11}^*},\ \tilde{D}_{12} = \frac{D_{12}^*}{D_{11}^*},\quad \tilde{D}_{22}^* = \frac{D_{22}^*}{D_{11}^*},\quad \tilde{D}_{66} = \frac{D_{66}^*}{D_{11}^*},\ \tilde{M}_{ij} = \frac{M_{ij}}{\rho^* h a^2},\ \tilde{N}_{ij}^{(3)} = \frac{N_{ij}^{(3)}a^4}{D_{11}^*}, \end{aligned} \tag{11}$$

the nondimensional reduced equations are obtained as

$$\begin{aligned} &\tilde{M}_H\ddot{\tilde{w}}_0(t) + \tilde{K}_H\tilde{w}_0(\tilde{t}) + \sum_{i=1}^{N}\tilde{M}_i(\ddot{\tilde{w}}_0(t) + \ddot{\tilde{z}}_{i0}(\tilde{t})) = 0, \\ &\tilde{M}_i(\ddot{\tilde{z}}_{i0}(t) + \ddot{\tilde{w}}_0(t)) + \tilde{K}_i\tilde{z}_{i0}(t) + \tilde{N}_i^{(3)}\tilde{z}_{i0}^3(t) = 0, \quad i = 1,\dots,N \end{aligned} \tag{12}$$

where

$$\tilde{M}_H = \tilde{A}(\tilde{k}_1,\tilde{k}_2), \quad \tilde{K}_H = \tilde{A}(\tilde{k}_1,\tilde{k}_2)\left[\tilde{k}_1^4 + \tilde{k}_1^2\tilde{k}_2^2 2(\tilde{D}_{12}+2\tilde{D}_{66}) + \tilde{k}_2^4\tilde{D}_{22}\right] \tag{13}$$

and

$$\tilde{A}(\tilde{k}_1,\tilde{k}_2) = \frac{4\sqrt{3}\sin\left(\frac{\tilde{k}_1}{2}\right)\sin\left(\frac{1}{4}\left(\tilde{k}_1+\sqrt{3}\tilde{k}_2\right)\right)}{\tilde{k}_1\left(\tilde{k}_1+\sqrt{3}\tilde{k}_2\right)}. \tag{14}$$

The nondimensional wave numbers $\tilde{k}_1, \tilde{k}_2$ within the Irreducible Brillouin zone (IBZ) exhibit the following ranges (see the first plot in Fig. 3): **ΓX**, **XM** and **MΓ**. The wave number vector (k_1, k_2) should lie within the triangular domain formed by the three

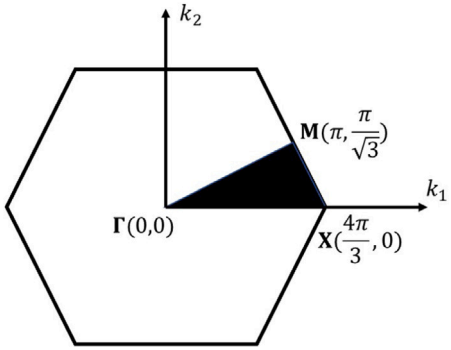

Fig. 3. The irreducible Brillouin zone.

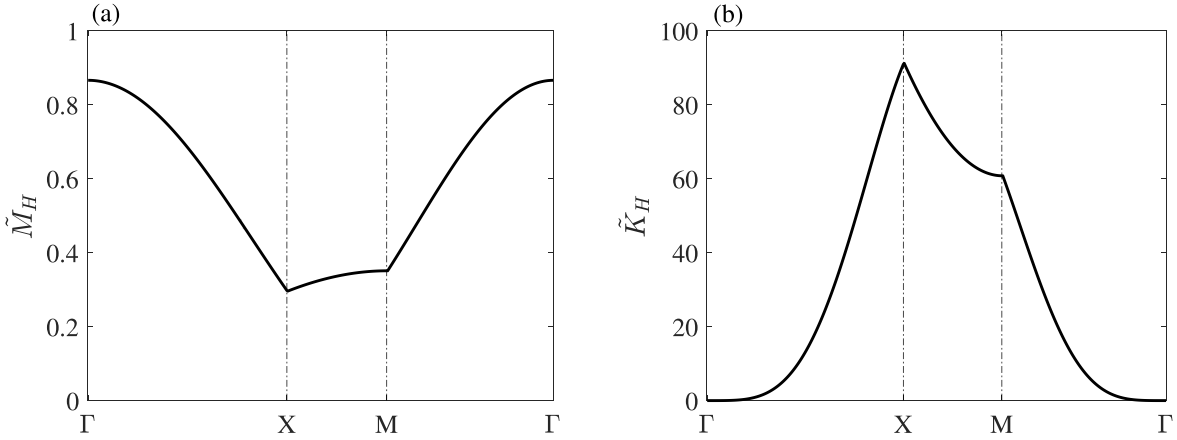

Fig. 4. (a) The effective mass and (b) stiffness of the plate as function of wave numbers.

points $(\mathbf{\Gamma}, \mathbf{X}, \mathbf{M})$. The effective mass and stiffness of the plate, with the material and geometric parameters shown in Section 5, versus different wave numbers are shown in Fig. 4 (a, b), respectively.

3. Linear dispersion functions and eigenvectors

For the metamaterial lattice with an array of equally spaced single-dof resonators (i.e., $N = 1$, so that the subscripts in $\tilde{M}_i$, $\tilde{K}_i$, $\tilde{N}_i^{(3)}$ can be dropped), wave equations (12) read:

$$\begin{bmatrix} \tilde{M}_H(\tilde{k}_1, \tilde{k}_2) + \tilde{M} & \tilde{M} \\ \tilde{M} & \tilde{M} \end{bmatrix} \begin{bmatrix} \ddot{\tilde{w}}_0(t) \\ \ddot{\tilde{z}}_0(t) \end{bmatrix} + \begin{bmatrix} \tilde{K}_H(\tilde{k}_1, \tilde{k}_2) & 0 \\ 0 & \tilde{K} \end{bmatrix} \begin{bmatrix} \tilde{w}_0(t) \\ \tilde{z}_0(t) \end{bmatrix} = \begin{bmatrix} 0 \\ -\tilde{N}^{(3)} \tilde{z}_0^3(t) \end{bmatrix}, \tag{15}$$

The solution of the linear problem can be sought by letting $w_0(t) = We^{i\omega t}$ and $\tilde{z}_0(t) = Ze^{i\omega t}$, where W and Z are constant coefficients. Thus, the ensuing eigenvalue problem is expressed as:

$$(\tilde{\mathbf{K}} - \omega^2 \tilde{\mathbf{M}})\boldsymbol{\phi} = \mathbf{0}, \tag{16}$$

where the column vector $\boldsymbol{\phi} = (W, Z)$ denotes the eigenvector and the mass and stiffness matrices are given by

$$\tilde{\mathbf{M}} = \begin{bmatrix} \tilde{M}_H(\tilde{k}_1, \tilde{k}_2) + \tilde{M} & \tilde{M} \\ \tilde{M} & \tilde{M} \end{bmatrix} \quad \text{and} \quad \tilde{\mathbf{K}} = \begin{bmatrix} \tilde{K}_H(\tilde{k}_1, \tilde{k}_2) & 0 \\ 0 & \tilde{K} \end{bmatrix}. \tag{17}$$

Setting the determinant of the coefficient matrix in Eq. (16) to zero yields the linear dispersion equation:

$$\det(\tilde{\mathbf{K}} - \omega^2 \tilde{\mathbf{M}}) = 0, \tag{18}$$

whose roots denoted by ω^- and ω^+ describe the frequencies of the low-frequency propagation mode $\boldsymbol{\phi}^-$ (acoustic mode) and the high-frequency propagation mode $\boldsymbol{\phi}^+$ (optical mode). Fig. 5 shows the linear dispersion properties of the bare plate (the relevant parameters are provided in Section 5) and the plate with resonators. The stop band, which is formed between the acoustic and optical frequencies, is highlighted in gray.

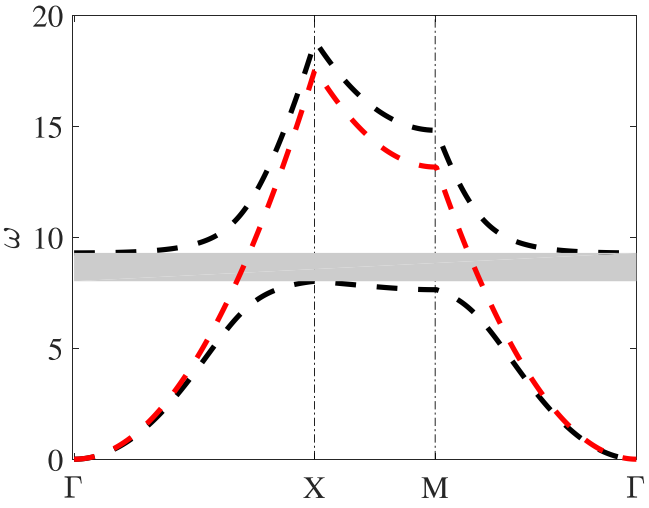

Fig. 5. The dispersion curves for the bare plate (red line) and plate with single-dof linear resonators (black lines) with $\tilde{M} = 0.146$ and $\tilde{K} = 10.79$. (For interpretation of the references to color in this figure legend, the reader is referred to the web version of this article.)

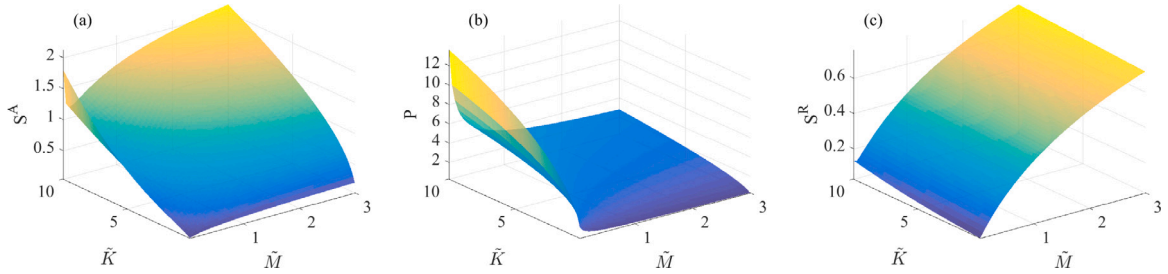

Fig. 6. (a) The linear stop band size $S^A = \min(\omega^+) - \max(\omega^-)$; (b) the linear absolute stop band position $P = (\min(\omega^+) + \max(\omega^-))/2$; (c) the linear relative stop band size $S^R = S^A/P$, versus $\tilde{M}$ and $\tilde{K}$.

The limit values of the frequencies across the boundaries of the IBZ are found in closed form. The formulas to find these values are provided below across each range (the full expressions are shown in Appendix B):

Γ – X :

$$\max(\omega^-) = \omega^-(\tilde{k}_1 = 4\pi/3, \tilde{k}_2 = 0), \quad \min(\omega^+) = \omega^+(\tilde{k}_1 = 0, \tilde{k}_2 = 0) \tag{19}$$

X – M :

$$\max(\omega^-) = \omega^-(\tilde{k}_1 = 4/3\pi, \tilde{k}_2 = 0), \quad \min(\omega^+) = \omega^+(\tilde{k}_1 = \pi, \tilde{k}_2 = \pi/\sqrt{3}) \tag{20}$$

M – Γ :

$$\max(\omega^-) = \omega^-(\tilde{k}_1 = \pi, \tilde{k}_2 = \pi/\sqrt{3}), \quad \min(\omega^+) = \omega^+(\tilde{k}_1 = 0, \tilde{k}_2 = 0). \tag{21}$$

An example with a given choice of the metamaterial system parameters (provided in Section 5) is shown here, the maximum acoustic frequency is obtained for $(\tilde{k}_1^A = 4\pi/3, \tilde{k}_2^A = 0)$ and the minimum optical frequency is found for $(\tilde{k}_1^O = 0, \tilde{k}_2^O = 0)$. The absolute stop band size is obtained as $S^A = \min(\omega^+) - \max(\omega^-)$. The stop band central frequency, which indicates the position of the stop band, is expressed by $P = (\min(\omega^+) + \max(\omega^-))/2$. The relative stop band size is defined by $S^R = S^A/P$. Fig. 6 shows the linear stop band size S^A, the central frequency P, and the relative stop band size S^R versus different choices of resonator parameters $\tilde{M}$ and $\tilde{K}$. The results highlight that when the resonators become heavier, the linear stop band will be enlarged but in the lower frequency range, and when the spring becomes stiffer, the stop band will have large width and appear in the high frequency range. When looking at the variation of the relative stop band size S^R upon variations of $\tilde{M}$ and $\tilde{K}$, it is found that the resonators should be heavy to have large values of the relative stop band size. These results facilitate the (linear) design process of the resonators parameters based on the stop band characteristic requirements.

Variations of the components of the acoustic and optical eigenvectors with the wave number are reported in Fig. 7. The well-known property holding for the acoustic mode being an in-phase mode and the optical mode being an out-of-phase mode is shown.

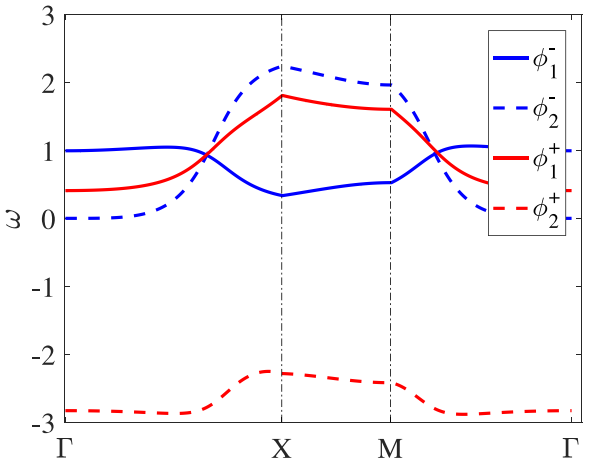

Fig. 7. Acoustic and optical eigenvectors components versus the wave number, for $\tilde{M} = 0.146$ and $\tilde{K} = 10.79$.

4. Nonlinear asymptotic solution

In this section, the method of multiple scales [34] is employed to analyze the nonlinear wave properties of metamaterials. As mentioned, the method of multiple scales is a classical tool for nonlinear asymptotic analysis and it is widely used also for the study of metamaterials (see, e.g., [28,36,39,40,48]). Let $\mathbf{u} = (\tilde{w}_0, \tilde{z}_{01}, \dots, \tilde{z}_{0N})$ be the vector collecting all plate and resonators coordinates so that Eq. (15) can be written in matrix-valued form as

$$\mathbf{M}\ddot{\mathbf{u}} + \mathbf{K}\mathbf{u} = \mathbf{N}(\mathbf{u}, \mathbf{u}, \mathbf{u}), \tag{22}$$

where $\mathbf{N}(\mathbf{u}, \mathbf{u}, \mathbf{u})$ represents the nonlinear part of the resonators restoring forces. By employing the mass-normalized modal matrix $\mathbf{\Phi}$ (which is equal to $[\boldsymbol{\phi}^-, \boldsymbol{\phi}^+]$ for one resonator case with eigenvectors $\boldsymbol{\phi}^\pm = (\phi_1^\pm, \phi_2^\pm)$), and by introducing the modal coordinate transformation $\mathbf{u} = \mathbf{\Phi}\mathbf{q}$, with $\mathbf{q} = (q_1, q_2)$ playing the role of principal coordinates vector, the following equation is obtained:

$$\mathbf{M}\mathbf{\Phi}\ddot{\mathbf{q}} + \mathbf{K}\mathbf{\Phi}\mathbf{q} = \mathbf{N}(\mathbf{\Phi}\mathbf{q}, \mathbf{\Phi}\mathbf{q}, \mathbf{\Phi}\mathbf{q}), \tag{23}$$

which, upon pre-multiplication by $\mathbf{\Phi}^\top$, yields:

$$\ddot{\mathbf{q}} + \mathbf{\Lambda}\mathbf{q} = \mathbf{c}(\mathbf{q}, \mathbf{q}, \mathbf{q}) \tag{24}$$

with $\mathbf{\Lambda} = \mathrm{diag}(\omega^{-2}, \omega^{+2})$ and

$$\mathbf{c}(\mathbf{q}, \mathbf{q}, \mathbf{q}) = \mathbf{\Phi}^\top \mathbf{N}(\mathbf{\Phi}\mathbf{q}, \mathbf{\Phi}\mathbf{q}, \mathbf{\Phi}\mathbf{q}) = \mathbf{\Phi}^\top \begin{bmatrix} 0 \\ -\tilde{N}^{(3)}(\boldsymbol{\phi}_2^\top \boldsymbol{q})(\boldsymbol{\phi}_2^\top \boldsymbol{q})(\boldsymbol{\phi}_2^\top \boldsymbol{q}) \end{bmatrix}, \tag{25}$$

where $\boldsymbol{\phi}_1 = \mathbf{\Phi}^\top \cdot \mathbf{e}_1$ and $\boldsymbol{\phi}_2 = \mathbf{\Phi}^\top \cdot \mathbf{e}_2$ are the vectors collecting the first and second rows of the mass-normalized modal matrix $\mathbf{\Phi}$, respectively; $\mathbf{e}_1 = (1, 0)$ and $\mathbf{e}_2 = (0, 1)$.

By making use of a small book-keeping nondimensional parameter denoted by ε, the method of multiple scales is employed to express the solution as a series of ε where each term is function of two time scales $T_j = \varepsilon^j t$ for $j = 0, 2$ according to

$$\mathbf{q} = \varepsilon \mathbf{q}_1(T_0, T_2) + \varepsilon^3 \mathbf{q}_2(T_0, T_2) + O(\varepsilon^5). \tag{26}$$

By taking into the change of time variables, the derivatives with respect to the actual fast time variable are expressed as: $\partial(\cdot)/\partial t = D_0 + \varepsilon^2 D_2$, and $\partial^2(\cdot)/\partial t^2 = D_0^2 + 2\varepsilon^2 D_0 D_2$, where $D_j(\cdot) = \partial(\cdot)/\partial T_j$. By equating to zero all terms of like powers of ε, the following hierarchy of problems is obtained:

Order(ε) :

$$D_0^2 \mathbf{q}_1 + \mathbf{\Lambda}\mathbf{q}_1 = \mathbf{0}, \tag{27a}$$

Order(ε^3) :

$$D_0^2 \mathbf{q}_2 + \mathbf{\Lambda}\mathbf{q}_2 = -2D_0 D_2 \mathbf{q}_1 + \mathbf{c}(\mathbf{q}_1, \mathbf{q}_1, \mathbf{q}_1), \tag{27b}$$

where the second perturbation problem was neglected because the complex-valued oscillation amplitudes $A^\pm$ do not depend on the slow time scale $T_1 = \varepsilon^2 t$ [28,38,49].

We only focus on the case of one resonator per unit cell; hence, the solution of the generating problem given by Eq. ((27)a) can be expressed in the form:

$$\mathbf{q}_1 = \begin{bmatrix} q_1^- \\ q_1^+ \end{bmatrix} = \begin{bmatrix} A^-(T_2)e^{i\omega^- T_0} + c.c. \\ A^+(T_2)e^{i\omega^+ T_0} + c.c. \end{bmatrix} \tag{28}$$

where the superscripts $\}\} - \varepsilon$ and $\}\} + \varepsilon$ describe the low-frequency (acoustic) mode and the high-frequency (optical) mode, respectively. The cubic perturbation problem expressed by Eq. ((27)b) contains resonant terms due to the cubic nonlinearity which would cause secular terms in the solution if not removed. By enforcing the solvability condition and assuming that the frequencies ω^- and ω^+ are away from the condition $\omega^+ \approx 3\omega^-$ so as to prevent the onset of a 3:1 internal resonance, one finally obtains:

$$\begin{aligned} 2i\omega^- D_2 A^- &= \boldsymbol{\phi}^{-\top} \begin{bmatrix} 0 \\ -\tilde{N}^{(3)}(3\phi_2^{-3} A^{-2}\bar{A}^- + 6\phi_2^- \phi_2^{+2} A^- A^+ \bar{A}^+) \end{bmatrix}, \\ 2i\omega^+ D_2 A^+ &= \boldsymbol{\phi}^{+\top} \begin{bmatrix} 0 \\ -\tilde{N}^{(3)}(3\phi_2^{+3} A^{+2}\bar{A}^+ + 6\phi_2^+ \phi_2^{-2} A^+ A^- \bar{A}^-) \end{bmatrix}. \end{aligned} \tag{29}$$

To obtain Eq. (29) in real-valued form, one needs to express $A^\pm$ in polar form as

$$A^\pm(T_2) = \tfrac{1}{2} a^\pm(T_2)\exp(i\theta^\pm(T_2)), \tag{30}$$

where $a^\pm$ and $\theta^\pm$ denote the unknown amplitude and phase of the optical and acoustic modes, respectively. Substituting Eq. (30) into Eq. (29) and separating real and imaginary parts in Eq. (29) yields:

$$a^{\pm\prime} = 0, \quad \theta^{\pm\prime} = \frac{\tilde{N}^{(3)}(3\phi_2^{\pm 4} a^{\pm 2} + 6\phi_2^{\pm 2}\phi_2^{\mp 2} a^{\mp 2})}{8\omega^\pm}. \tag{31}$$

Finally, by re-absorbing ε in the amplitude definition, the nonlinear frequencies of the two wave modes are expressed as

$$\omega_{nl}^- = \omega^- + \frac{\tilde{N}^{(3)}(3\phi_2^{-4} a^{-2} + 6\phi_2^{-2}\phi_2^{+2} a^{+2})}{8\omega^-}, \quad \omega_{nl}^+ = \omega^+ + \frac{\tilde{N}^{(3)}(3\phi_2^{+4} a^{+2} + 6\phi_2^{+2}\phi_2^{-2} a^{-2})}{8\omega^+}. \tag{32}$$

The above equations describe the nonlinear, amplitude-dependent dispersion functions for the acoustic and optical modes. Note that the eigenvector components $\phi_j^\pm$ and the nonlinear coefficients depend on the wave numbers $\tilde{k}_1$, and $\tilde{k}_2$. Eq. (32) is a key result of the asymptotic approach since it unfolds the nonlinear wave propagation characteristics of the metamaterial, indicating that the acoustic and optical modes are not uncoupled in the dispersion functions. This result holds as far as the system is considered undamped. In addition, in Appendix C we show that a direct asymptotic treatment of the nonlinear equation of motion Eq. (1) together with the Floquet–Bloch solution ansatz at each order yields the same results as those obtained by assuming the Floquet–Bloch solution for the nonlinear system from the outset and projecting the equation onto the unit cell domain. This is true as far as the asymptotic treatment is arrested to within the first nonlinear order (i.e., here the cubic order) and is not aimed at a higher order approximation. For higher order approximations, the Floquet–Bloch solution ansatz has to be relaxed.

5. Numerical examples

Numerical examples are computed to discuss the effects of the resonator nonlinearity on the dispersion functions and to offer guidance towards the optimization of the resonators. The parameters of the honeycomb used for the numerical simulations are: characteristic length $a = 0.14$m, plate height $h = 0.005$m, plate density $\rho = 1150$ kg/m^3, Young's modulus $E = 2.2$ GPa, Poisson's ratio $\nu = 0.35$. The geometric parameters of the hexagon are: thickness $t_h = 0.001$m and side length $l_h = a \times \tan(\pi/6)$.

When applying the multiple scale approach, we assumed that the nonlinear part of the resonator restoring force F_{nl} should be smaller (of ε^3 order) than the linear restoring force F_{lin}. To this end, we set the condition that the ratio between F_{nl} and F_{lin} must be smaller than 1 in the whole range of nonlinearity coefficient. The conditions providing the amplitude bounds thus read:

$$\frac{F_{nl}^+}{F_{lin}^+} = \left|\frac{\phi_2^+ \tilde{N}^{(3)}(\phi_2^+ a^+ + \phi_2^- a^-)^3}{(\omega^+)^2 a^+}\right| < 1 \text{ and } \quad \frac{F_{nl}^-}{F_{lin}^-} = \left|\frac{\phi_2^- \tilde{N}^{(3)}(\phi_2^+ a^+ + \phi_2^- a^-)^3}{(\omega^-)^2 a^-}\right| < 1, \tag{33}$$

This set of conditions has the virtue of ensuring the validity of the asymptotic approach by preventing selection of exceedingly large values of the amplitudes as a function of the given nonlinearity coefficient.

5.1. Dispersion properties

Fig. 8(a) shows the comparison between the dispersion properties of the metamaterial with linear resonators with the properties of the metamaterial with nonlinear resonators. In the numerical test here considered, the modal amplitudes of the acoustic and optical modes were set to $a^- = 10^{-2}$ and $a^+ = 5 \times 10^{-3}$. To quantify the nonlinear effects on the stop band sizes, we introduce the function G as the ratio of the nonlinear stop band width to the corresponding linear stop band width, i.e.,

$$G = \frac{\min(\omega_{nl}^+) - \max(\omega_{nl}^-)}{\min(\omega^+) - \max(\omega^-)}. \tag{34}$$

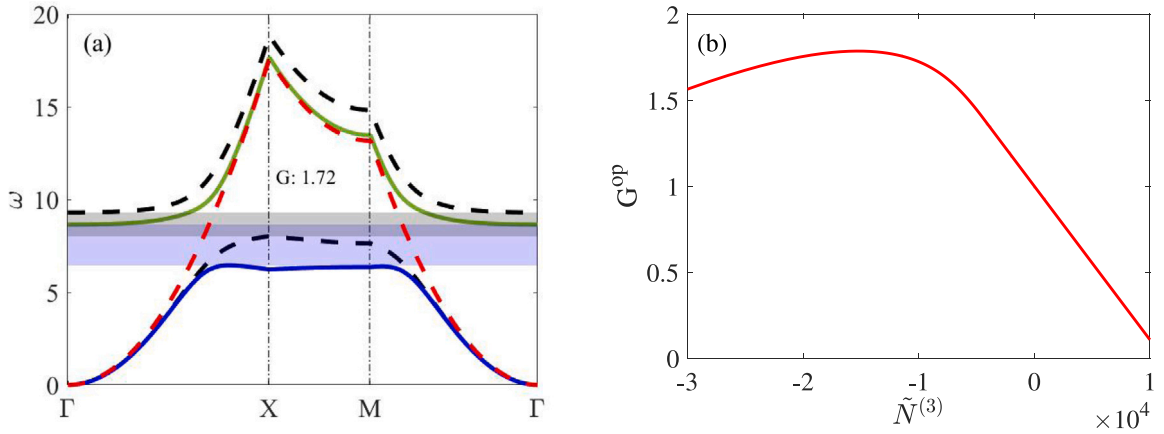

Fig. 8. (a) The dispersion curves of the metamaterial with the single-dof nonlinear resonator; the modal amplitudes are set to $a^- = 10^{-2}$ and $a^+ = 5 \times 10^{-3}$. The resonators parameters are: $\tilde{M} = 0.146, \tilde{K} = 10.79$, and the nonlinearity is set to $\tilde{N}^{(3)} = -10^4$. As in Fig. 5, the red and black dashed curves represent the dispersion properties of the plate without resonators and with linear resonators, respectively. The nonlinear optical and acoustic frequencies are shown by the blue and green curves, respectively. (b) The nonlinear stop band gain versus the nonlinearity coefficient $\tilde{N}^{(3)}$. (For interpretation of the references to color in this figure legend, the reader is referred to the web version of this article.)

In Fig. 8(a), compared to the linear stop band shown in gray, the nonlinear stop band, which is highlighted in light blue, gets shifted to lower frequencies due to the softening resonators having a cubic spring coefficient $\tilde{N}^{(3)} = -10^4$. At the same time, the stop band largely increases (by as much as 72%) when the nonlinearity is taken into account. Fig. 8(b) showing G versus $\tilde{N}^{(3)}$ highlights the fact that there exists an optimal value of the nonlinearity strength which yields the largest stop band size within the set range for a given selection of modal amplitudes (here $a^- = 10^{-2}$ and $a^+ = 5 \times 10^{-3}$).

The outcomes of the investigations into the nonlinearity of the resonators point out that the stop band size can be considerably enlarged by suitably choosing the type and strength of the nonlinearity. The next section will address the optimization of the resonators nonlinearity.

5.2. Design of the nonlinear resonators with certain targeted frequency

To enhance the band gap performance of the metamaterial with nonlinear resonators, one of the key problems is to determine whether the resonator should be hardening or softening. To solve this problem, the nonlinear terms in the dispersion functions yielding the nonlinear corrections to the linear stop band width can be expressed as:

$$Q = [\min(\omega_{nl}^+) - \max(\omega_{nl}^-)] - [\min(\omega^+) - \max(\omega^-)]. \tag{35}$$

The nonlinearity promotes a widening of the stop band when Q is positive definite. By assuming that the nonlinearity is not too large, the wave numbers $\tilde{k}_1^A = 4\pi/3$ and $\tilde{k}_2^A = 0$ leading to the maximum linear acoustic frequency and $\tilde{k}_1^O = 0$ and $\tilde{k}_2^O = 0$ leading to the minimum optical frequency will not change in the nonlinear case. Consequently, one can rewrite Q given by Eq. (35) as:

$$\begin{aligned} Q = {} & \tilde{N}^{(3)} \left[(2\phi_2^{+2}\phi_2^{-2}/\omega^+)|_{(\tilde{k}_1^O, \tilde{k}_2^O)} - (\phi_2^{-4}/\omega^-)|_{(\tilde{k}_1^A, \tilde{k}_2^A)} \right] a^{-2} \\ & + \tilde{N}^{(3)} \left[(\phi_2^{+4}/\omega^+)|_{(\tilde{k}_1^O, \tilde{k}_2^O)} - (2\phi_2^{+2}\phi_2^{-2}/\omega^-)|_{(\tilde{k}_1^A, \tilde{k}_2^A)} \right] a^{+2}, \end{aligned} \tag{36}$$

or, in more compact form, as

$$Q = \tilde{N}^{(3)}(\Gamma^- a^{-2} + \Gamma^+ a^{+2}) =: \tilde{N}^{(3)} \Lambda(a^-, a^+). \tag{37}$$

Eq. (37) embeds the key information that will guide the answer to the question of whether hardening or softening resonators should be selected. In other words, to ensure that the quadratic form Q given by Eq. (37) be positive regardless of the range of acoustic and optical amplitudes, one has to tune the resonators nonlinearity based on the constants $\Gamma^\pm$ (i.e., they are determined by the parameters of the resonators) and on the modal amplitudes $a^\pm$.

The goal is to determine suitable resonators parameters $(\tilde{M}, \tilde{K})$ such that the effective nonlinearity coefficients $\Gamma^\pm$ will result into one of the following conditions:

$$\Lambda(a^-, a^+) > 0 \text{ if } \tilde{N}^{(3)} > 0 \text{ or } \Lambda(a^-, a^+) < 0 \text{ if } \tilde{N}^{(3)} < 0 \tag{38}$$

for any combination of $a^\pm$, depending on the type of nonlinearity ($\tilde{N}^{(3)} > 0$ or $\tilde{N}^{(3)} < 0$). The inequalities given by Eq. (38) can be written as $\text{sign}(\Lambda \tilde{N}^{(3)}) = 1$. The best strategy is to seek conditions under which the type of nonlinearity of the resonators does

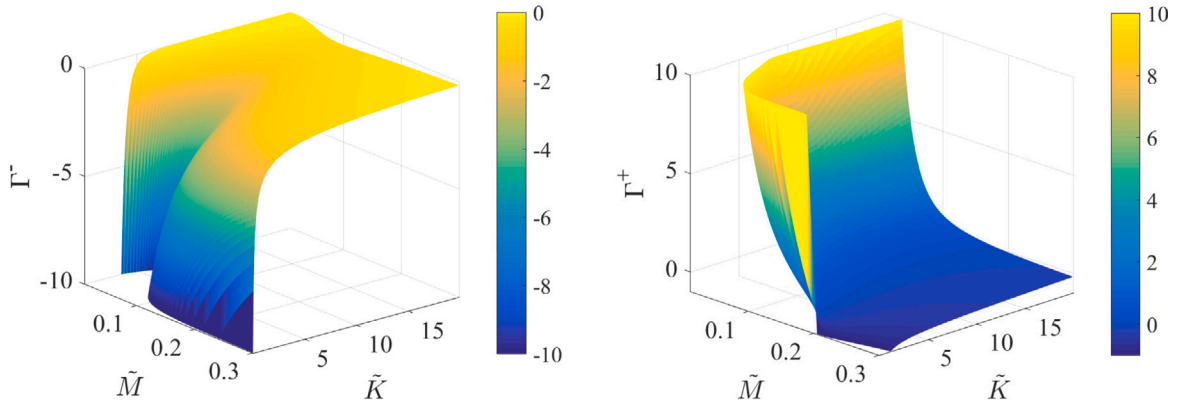

Fig. 9. Γ^- and Γ^+ versus $\tilde{M}$ and $\tilde{K}$.

not need to be tuned based on the modal amplitudes so as to overcome the drawback of adaptive nonlinearity in the resonators. Inequalities (38) are satisfied if Γ^- and Γ^+ meet one of the following conditions:

(1) Γ^- and Γ^+ are both positive with $\tilde{N}^{(3)} > 0$ (hardening),
(2) Γ^- and Γ^+ are both negative with $\tilde{N}^{(3)} < 0$ (softening),
(3) $|\Gamma^-| \gg |\Gamma^+|$ and a^- and a^+ are of the same order.
(4) $|\Gamma^-| \ll |\Gamma^+|$ and a^- and a^+ are of the same order.

To find where the parameters of the resonators satisfy one of the above conditions, we introduce the ratio between the effective nonlinearity coefficients as

$$\gamma = \Gamma^-/\Gamma^+. \tag{39}$$

Condition (3) comes from the fact that when $|\gamma| \gg 1$, it is $1/|\gamma| = O(\varepsilon)$ and by combining this fact with the asymptotic assumption $a^{\pm 2} = O(\varepsilon^2)$, one obtains:

$$\Lambda = (\Gamma^- a^{-2} + \Gamma^+ a^{+2}) = \Gamma^-(a^{-2} + \tfrac{1}{\gamma} a^{+2}) = \Gamma^-(O(\varepsilon^2) + O(\varepsilon^3)). \tag{40}$$

In another words, the sign of Λ is dictated by the sign of Γ^-. Similarly, condition (4) stems from the fact that under the assumption $|\gamma| \ll 1$, which can be stated as $\gamma = O(\varepsilon)$, one obtains:

$$\Lambda = (\Gamma^- a^{-2} + \Gamma^+ a^{+2}) = \Gamma^+(\gamma a^{-2} + a^{+2}) = \Gamma^+(O(\varepsilon^3) + O(\varepsilon^2)). \tag{41}$$

Thus, the sign of Λ is ruled by Γ^+. Fig. 9 shows variations of $\Gamma^\pm$ as function of $\tilde{M}$ and $\tilde{K}$.

In order to discuss the various scenarios, in terms of the above defined ratio, we can recognize the following conditions leading to the optimal resonators nonlinearity:

(1) $\gamma > 0$ and $\Gamma^- > 0$, entail $\tilde{N}^{(3)} > 0$ (hardening),
(2) $\gamma > 0$ and $\Gamma^- < 0$, entail $\tilde{N}^{(3)} < 0$ (softening),
(3a) $\text{sign}(\tilde{N}^{(3)}\Gamma^-) = 1$ and $\Gamma^- > 0$, thus, $\tilde{N}^{(3)} > 0$ (hardening),
(3b) $\text{sign}(\tilde{N}^{(3)}\Gamma^-) = 1$ and $\Gamma^- < 0$, thus, $\tilde{N}^{(3)} < 0$ (softening),
(4a) $\text{sign}(\tilde{N}^{(3)}\Gamma^+) = 1$ and $\Gamma^+ > 0$, thus, $\tilde{N}^{(3)} > 0$ (hardening),
(4b) $\text{sign}(\tilde{N}^{(3)}\Gamma^+) = 1$ and $\Gamma^+ < 0$, thus, $\tilde{N}^{(3)} < 0$ (softening).

In other words, when γ is positive, or when γ is negative and small in absolute value (i.e., $|\gamma| < 0.1$ to meet condition (3)) or negative and large in absolute value (i.e., $|\gamma| > 10$ to meet condition (4)), for almost all combinations of $a^\pm$, one should use a certain type of nonlinearity to obtain a positive Q. On the other hand, when $\gamma < 0$ and $0.1 < |\gamma| < 10$ (i.e., the effective nonlinearity coefficients are of the same order of magnitude), some combinations of $a^\pm$ will require a softening nonlinearity while other combinations will require hardening resonators for enhanced stop band. The drawback is that self-adaptive resonators should be designed to obtain enhanced performance.

Fig. 10 shows the contour plot of γ versus $\tilde{M}$ and $\tilde{K}$, the red and green curves show the bound along which $\gamma = -0.1$ or $\gamma = \pm 10$, thus, the parameter space spanned by $\tilde{M}$ and $\tilde{K}$ is divided into four regions, each of which is characterized by a certain type of optimal nonlinearity. In the plot, "H" means hardening, "S" means softening, and "A" represents adaptive nonlinearity, and the corresponding condition is also given for each region with certain type of optimal nonlinearity. Fig. 11 shows the final suggested type of resonator nonlinearity in the plane spanned by $\tilde{M}$ and $\tilde{K}$. Fig. 11 represents a design chart that can be exploited during the metamaterial design process.

When one has to design a new metamaterial with a certain targeted frequency, the results shown in Figs. 6 and 11 indicate the strategy to find the proper choice of mass $\tilde{M}$ and stiffness $\tilde{K}$ as well as the optimal type of resonators nonlinearity. After choosing optimal resonators nonlinearity, one still needs to carefully select the strength of the nonlinearity. The choice of $\tilde{N}^{(3)}$ should be optimized based on the range of modal amplitudes of the incoming waves, to obtain the largest stop band width.

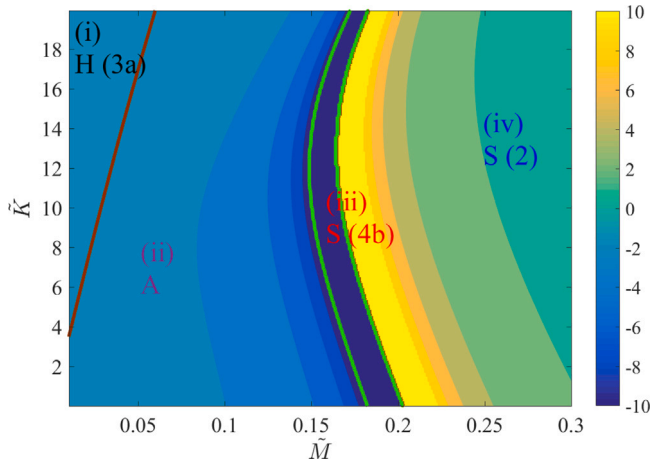

Fig. 10. Contour plot of γ versus $\tilde{M}$ and $\tilde{K}$. The red and green curves divide the parameter space into four regions where different types of optimal resonators nonlinearity should be employed to enlarge the stop band for all amplitudes $a^{\pm}$. H stands for hardening, A for self-adaptive, and S for softening. (For interpretation of the references to color in this figure legend, the reader is referred to the web version of this article.)

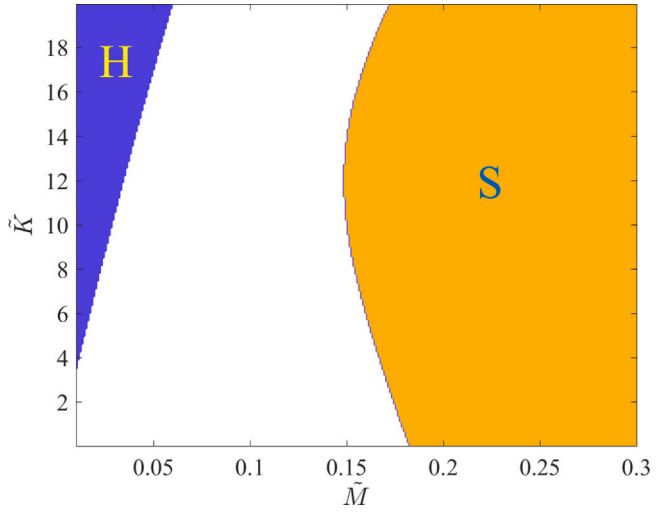

Fig. 11. Design chart with the suggested type of optimal resonator nonlinearity based on the values of $\tilde{M}$ and $\tilde{K}$.

Numerical example: target frequency $\bar{\omega} = 5$

An example is given here to show how to enlarge the stop band width by using optimal nonlinear resonators when the target frequency is set to $\bar{\omega} = 5$. From the results shown in Figs. 6 and 10, we select $\tilde{M} = 0.3$ and $\tilde{K} = 7.54$ thus $\bar{\omega} = 5$ in the linear stop band region and softening resonators are expected to provide an increased stop band width. With this choice of parameters, Fig. 12(a) shows the results in terms of optimal value $\tilde{N}^{(3)}$ for every combination of a^- and a^+ leading to the largest bandgap G. In the numerical search, the range of $a^{\pm}$ was set to [0, 0.01] and 100 grid points were selected; $\tilde{N}^{(3)}$ was investigated in the range $[-2, 2] \times 10^4$. Fig. 12(b) provides the corresponding maximum nonlinear stop band gain factor G for the found optimal values of the nonlinear coefficient in (a). It is shown that if the minimum value $\tilde{N}^{(3)} = -5 \times 10^3$ is selected, for every combination of modal amplitudes, the nonlinear stop band is always larger than the linear counterpart ($G^{op} > 1$). In practice, it is better to select values larger than the minimum value to have more considerable nonlinear effects, thus, in the next numerical study, we set $\tilde{N}^{(3)} = -10^4$.

To further investigate the sensitivity of the stop band gain factor, we show in Fig. 13 variation of G with the amplitudes $a^{\pm}$ for the honeycomb embedding resonators with the nonlinearity coefficient set to $\tilde{N}^{(3)} = -10^4$. The amplitudes a^+ and a^- are varied in the range $[0, 0.01]$ within a grid of 100 points. It is found that in all situations, the selected softening nonlinearity can act to considerably increase the stop band by as much as 60%. One can thus conclude that, with the softening nonlinearity involved, the performance of the metamaterial is always enhanced for any incoming wave exciting both the acoustic or optical mode at moderately large amplitudes.

Finally, we consider the dispersion curves for certain modal amplitudes to check whether the nonlinear effects are consistent with the expectations. The nonlinearity is chosen again to be $\tilde{N}^{(3)} = -10^4$ as in the optimization results obtained in Fig. 12, while

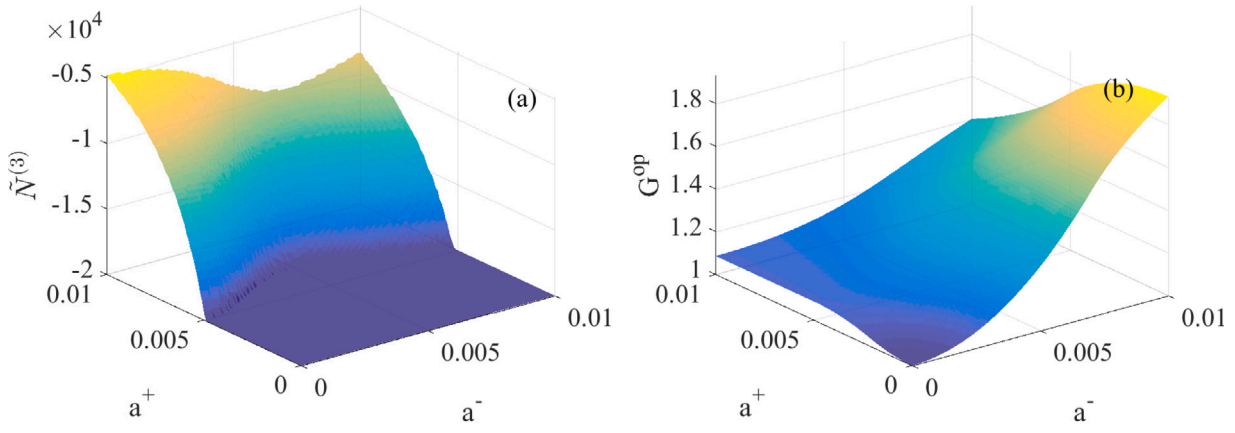

Fig. 12. (a) The optimization results about the selection of $\tilde{N}^{(3)}$ in terms of modal amplitudes $a^{\pm}$ leading to the largest bandgap size. (b) The corresponding maximum stop band size when choosing the nonlinearity coefficients given in (a).

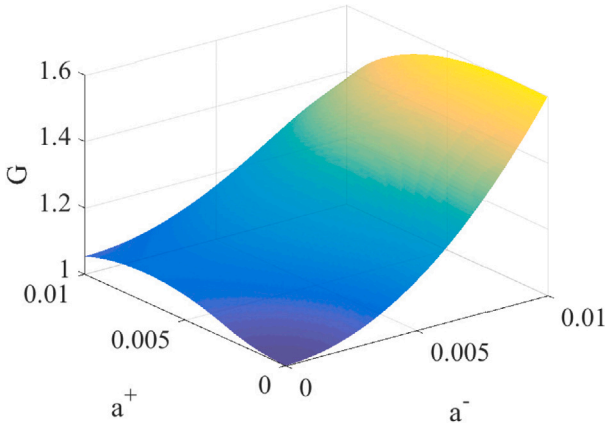

Fig. 13. Variation of the nonlinear stop band gain factor G for the metamaterial with softening resonators in terms of the modal amplitudes a^{-} and a^{+} with $\tilde{N}^{(3)} = -10^4$.

the modal amplitudes are set to (a) $a^{-} = a^{+} = 5 \times 10^{-3}$, (b) $a^{-} = a^{+} = 8 \times 10^{-3}$, (c) $a^{-} = 10^{-2}, a^{+} = 5 \times 10^{-3}$, respectively. Fig. 14 shows the dispersion curves for the three cases. It is found that the nonlinear stop bands (denoted by blue and green curves) are significantly larger than the linear counterparts (described by black dashed curve), with the target frequency $\bar{\omega} = 5$ still within the nonlinear stop band range.

In summary, the optimization process reveals the possibility that, by a proper selection of the nonlinear characteristics of the resonators, the nonlinear stop band can be significantly enlarged, leading to a surprising enhancement of the energy absorption performance of the metamaterial.

5.3. Numerical validation of the stop band behavior with damping

A numerical example is further provided to verify the stop band behavior in the presence of damping of the hosting honeycomb. In this numerical example, we consider the metamaterial subject to a harmonic excitation for various frequencies and in the range of wave numbers spanning the boundary of the IBZ ($\mathbf{\Gamma} - \mathbf{X}$, $\mathbf{X} - \mathbf{M}$, $\mathbf{M} - \mathbf{\Gamma}$). The resonators parameters are set to $\tilde{M} = 0.3$ and $\tilde{K} = 7.54$, as in the previous section. The equations of motion of the metamaterial system with damping are given by:

$$\begin{bmatrix} \tilde{M}_H(\tilde{k}_1,\tilde{k}_2) + \tilde{M} & \tilde{M} \\ \tilde{M} & \tilde{M} \end{bmatrix} \begin{bmatrix} \ddot{\tilde{w}}_0(t) \\ \ddot{\tilde{z}}_0(t) \end{bmatrix} + \begin{bmatrix} \tilde{K}_H(\tilde{k}_1,\tilde{k}_2) & 0 \\ 0 & \tilde{K} \end{bmatrix} \begin{bmatrix} \tilde{w}_0(t) \\ \tilde{z}_0(t) \end{bmatrix} + \begin{bmatrix} \tilde{C}_H(\tilde{k}_1,\tilde{k}_2) & 0 \\ 0 & \tilde{C} \end{bmatrix} \begin{bmatrix} \dot{\tilde{w}}_0(t) \\ \dot{\tilde{z}}_0(t) \end{bmatrix} = \begin{bmatrix} 0 \\ -\tilde{N}^{(3)}\tilde{z}_0^3(t) \end{bmatrix} + \begin{bmatrix} \tilde{F}\sin(\tilde{\omega}_{ex}t) \\ 0 \end{bmatrix}, \tag{42}$$

where $\tilde{F}$ is the external force amplitude, $\tilde{\omega}_{ex}$ is the excitation frequency which spans the range from 0.1 to 20 with step set to 0.2 (reduced to 0.02 near the boundary of the stop bands), while the system damping is set to be: $\tilde{C}_H = 2\tilde{\zeta}\sqrt{\tilde{K}_H/\tilde{M}_H}\tilde{A}(k_1,k_2)$ with

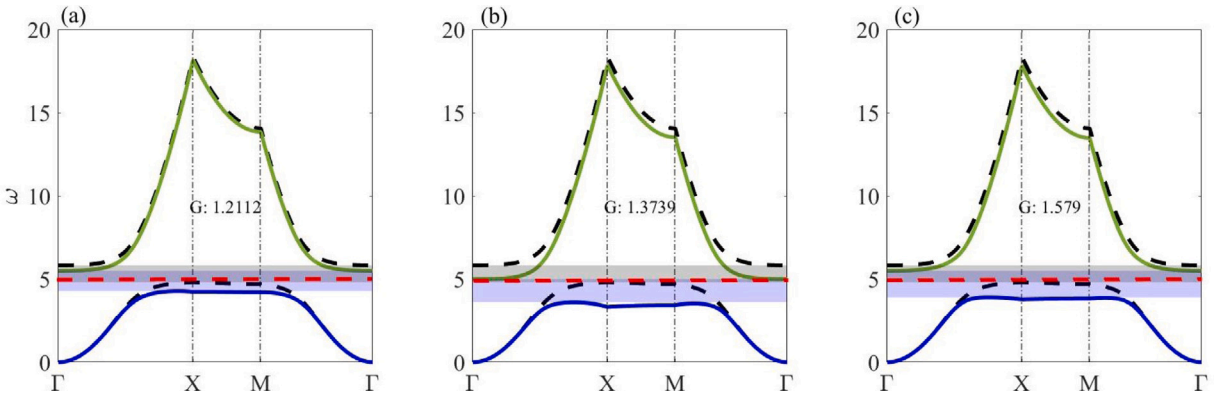

Fig. 14. The nonlinear dispersion functions with nonlinear coefficient $N^{(3)} = -10^4$ and the modal amplitudes set to : (a) $a^- = a^+ = 5\times10^{-3}$, (b) $a^- = a^+ = 8\times10^{-3}$, (c) $a^- = 10^{-2}, a^+ = 5\times10^{-3}$. The red dashed curve here indicates the target frequency. (For interpretation of the references to color in this figure legend, the reader is referred to the web version of this article.)

$\tilde{\zeta} = 0.05$ and $\tilde{C} = 0$. The fourth-order Runge–Kutta method (function "ode45" in Matlab) is used to integrate the equation of motion yielding the time response.

We collect the maximum displacement amplitudes of the plate at steady-state for every selection of wave numbers and excitation frequency. The results are shown in Fig. 15 in terms of contour plots where the horizontal axis denotes the wave number, the vertical axis indicates the non-dimensional harmonic excitation frequency, while the steady-state displacement amplitude levels are represented by different colors; in particular, bright yellow means amplitudes beyond 5×10^{-3}, which is 14% the nondimensional plate thickness h/a. Correspondingly for the damped wave propagation scenario here considered, the stop band is defined as the region where the wave amplitude is sufficiently small ($< 5\times10^{-3}$) across all wave numbers and excitation frequencies. Fig. 15(a) shows that the dispersion curves for the metamaterial with linear resonators, here described by dashed black lines, fully matches the numerically obtained time response (alongside the middle of the yellow range), and that the stop band region goes from 4.80 to 5.70. On the other hand, Fig. 15(b) shows the nonlinear resonators case with $\tilde{N}^{(3)} = -2000$, not chosen as large as in the last section to avoid convergence problems. The newly formed stop band region highlighted by the red dashed box, due to the nonlinearity and damping effects, gets enlarged between $\tilde{\omega}_{ex} = 4.32$ and 5.42. Hence, $G = (5.42 - 4.32)/(5.70 - 4.80) = 1.22$ indicates that the stop band width increases by 22% thanks to the resonators nonlinearity also in the presence of damping. The corresponding 3D frequency-wave number response plots for the linear and nonlinear cases are shown in parts (c, d), respectively, to provide a more effective graphical representation of the damped stop band.

6. Conclusions

In this paper, the nonlinear wave properties of honeycombs embedding spider web-like resonators are studied. The wave propagation equations were derived making use of the Floquet–Bloch quasi-periodicity ansatz and the projection method. The nonlinear dispersion properties were obtained in closed form employing the method of multiple scales. Numerical examples showed that the stop band width of the honeycomb can be significantly enhanced by the presence of suitable nonlinear resonators.

In the first part of this work, the linear dispersion properties of the honeycomb metamaterials were addressed by investigating the relationship between the linear stop band characteristics (size and position) and the variation of resonator mass and stiffness. The main contribution consists in the full range of analytical studies into the effects of the nonlinearity of the resonators embedded into the honeycomb metamaterial. It has been proved that the nonlinearity of the resonators can be designed to exert great beneficial effects on the dispersion properties enhancing the frequency range where wave propagation is stopped.

The extensive numerical studies based on the analytical solutions helped streamlining an optimal design approach which determines the type of nonlinearity as a function of the mass and stiffness of the resonators. The optimal nonlinear resonators design leads to an enlarged stop band for any modal amplitude governing the acoustic and optical modes. First, the targeted stop band frequency is chosen and the corresponding suitable linear resonators properties are defined (i.e., mass and stiffness). Subsequently, the optimal nonlinearities of the resonators are determined thanks to a behavior chart depicting regions of optimal softening, hardening or adaptive nonlinearity. Time domains simulations were carried out to validate the existence of the stop band and to show how the numerically obtained stop band gets enlarged under the simultaneous presence of hosting honeycomb damping and resonators nonlinearity.

The conducted analytical computations of the nonlinear dispersive waves and the numerical sensitivity optimization studies within the nonlinear vibratory regime provide a comprehensive outlook into the dispersion properties of the nonlinear metamaterial, and the opportunities offered by the exploitation of the resonator nonlinearity to enhance the wave propagation control capability of the metamaterial.

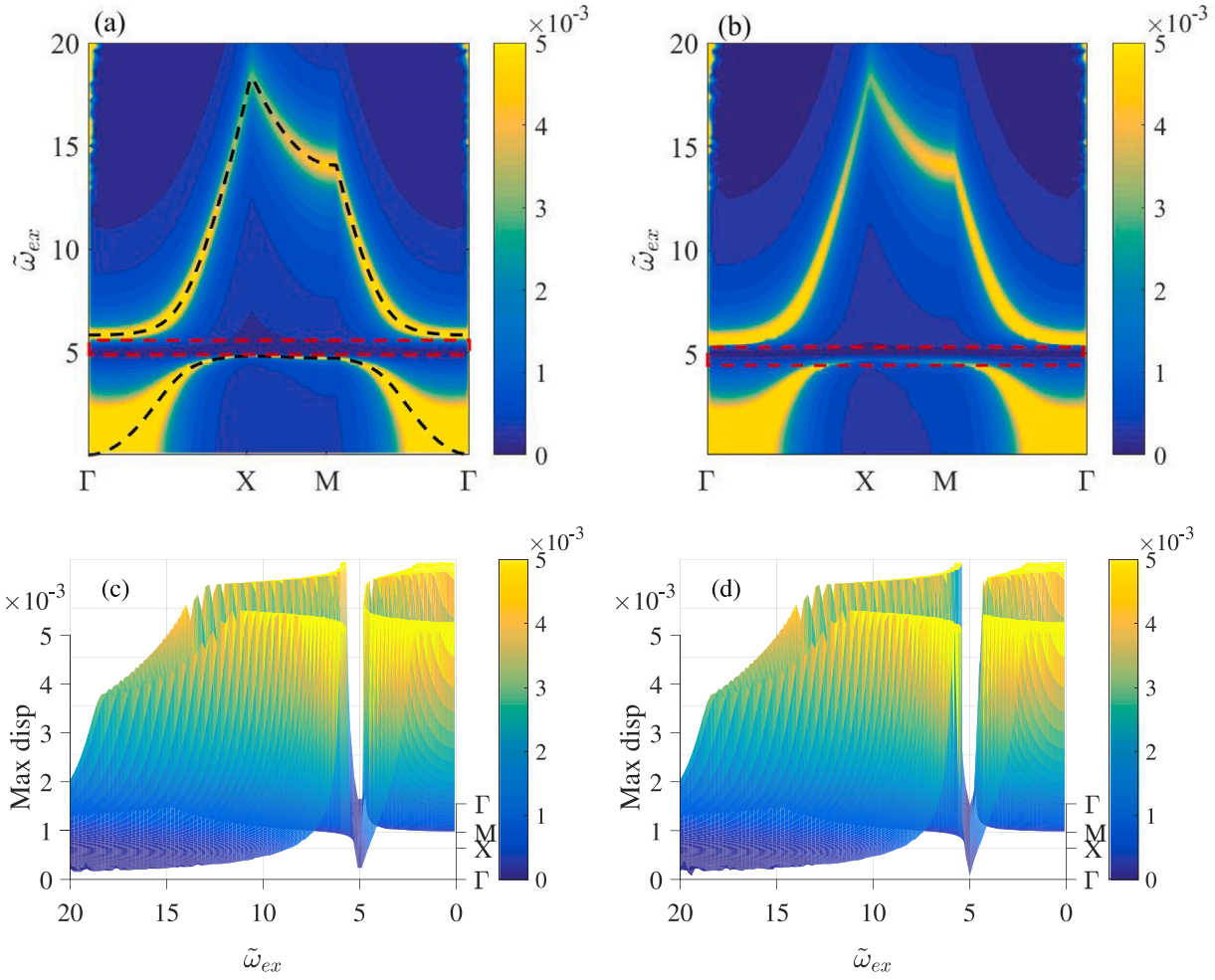

Fig. 15. (a, b) Contour plots showing the displacement amplitudes of the plate at steady-state for the metamaterial subject to harmonic excitation ($\tilde{F} = 0.03$) and (c, d) the corresponding 3D plots. The dashed lines are the analytical predictions of the linear dispersion curves. In parts (a, c) the resonators are linear (i.e., $\tilde{N}^{(3)} = 0$), in parts (b, c) the resonators are nonlinear with $\tilde{N}^{(3)} = -2 \times 10^3$.

Declaration of competing interest

The authors declare that they have no known competing financial interests or personal relationships that could have appeared to influence the work reported in this paper.

Data availability

Data will be made available on request.

Acknowledgments

This work was partially supported by a MIUR (Italian Ministry of Education, Scientific Research and University) Grant 2017L7X3CS_002 and by the European Office of Aerospace Research and Development/Air Force Office of Scientific Research under Grant N. FA8655-20-1-7025.

Appendix A. The orthotropic bending coefficients and the density of the equivalent plate

The orthotropic bending coefficients $D_{11}^*, D_{12}^*, D_{22}^*, D_{66}^*$ and the density $\rho^\star$ of the equivalent plate read [46]:

$$\begin{aligned}
D_{11}^* &= \frac{0.023958 E h^3 t_h \left(l_h^2 + (1.5\nu + 5.4) t_h^2\right)^2}{l_h^5 + l_h^3 (1.5\nu + 3.4) t_h^2} \\
D_{12}^* &= \frac{0.023958 E h^3 t_h \left(l_h^2 + (1.5\nu + 1.4) t_h^2\right) \left(l_h^2 + (1.5\nu + 5.4) t_h^2\right)}{l_h^5 + l_h^3 (1.5\nu + 3.4) t_h^2} \\
D_{22}^* &= \frac{0.023958 E h^3 t_h \left(l_h^2 + (1.5\nu + 5.4) t_h^2\right)^2}{l_h^5 + l_h^3 (1.5\nu + 3.4) t_h^2} \\
D_{66}^* &= \frac{0.0475 E h^3 t_h^3}{l_h^3} \\
\rho^\star &= \frac{t_h / l_h (h / l_h + 2)}{2 \cos\theta (h / l_h + \sin\theta)} \rho
\end{aligned} \tag{A.1}$$

where E is the Young's modulus and ν is the Poisson's ratio.

Appendix B. The limit values for the linear dispersion function

•Γ – X:

$$\begin{aligned}
\max(\omega^-) =& \omega^-(\tilde{k}_1 = 4\pi/3, \tilde{k}_2 = 0) = \Bigg(\frac{1}{162\tilde{M}} \Big(256\tilde{M}\pi^4 + \tilde{K}(81 + 16\sqrt{3}\tilde{M}\pi^2) - \\
& \sqrt{(65536\tilde{M}^2\pi^8 + 512\tilde{K}\tilde{M}\pi^4(16\sqrt{3}\tilde{M}\pi^2 - 81) + 3\tilde{K}^2(2187 + 864\sqrt{3}\tilde{M}\pi^2 + 256\tilde{M}^2\pi^4))} \Big) \Bigg)^{\frac{1}{2}} \\
\min(\omega^+) =& \omega^+(\tilde{k}_1 = 0, \tilde{k}_2 = 0) = \sqrt{\left(\tilde{K}(3 + 2\sqrt{3}\tilde{M}) + \sqrt{3}\sqrt{\tilde{K}^2(3 + 4\tilde{M}(\sqrt{3} + \tilde{M}))} \right) / (6\tilde{M})}
\end{aligned} \tag{B.1}$$

•X – M:

$$\begin{aligned}
\max(\omega^-) =& \omega^-(\tilde{k}_1 = 4/3\pi, \tilde{k}_2 = 0) = \Bigg(\frac{1}{162\tilde{M}} \Big(256\tilde{M}\pi^4 + \tilde{K}(81 + 16\sqrt{3}\tilde{M}\pi^2) - \\
& \sqrt{(65536\tilde{M}^2\pi^8 + 512\tilde{K}\tilde{M}\pi^4(16\sqrt{3}\tilde{M}\pi^2 - 81) + 3\tilde{K}^2(2187 + 864\sqrt{3}\tilde{M}\pi^2 + 256\tilde{M}^2\pi^4))} \Big) \Bigg)^{\frac{1}{2}} \\
\min(\omega^+) =& \omega^+(\tilde{k}_1 = \pi, \tilde{k}_2 = \pi/\sqrt{3}) \\
=& \Bigg(\frac{1}{36\tilde{M}} \Big(18\tilde{K} + \tilde{M}\pi^2(3\sqrt{3}\tilde{K} + 18\pi^2 + 12D_1\pi^2 + 2D_2\pi^2) + \\
& \frac{3}{2}\sqrt{-64(9 + 6\tilde{D}_1 + \tilde{D}_2)\tilde{K}\tilde{M}\pi^4 + \frac{4}{9}(2(9 + 6\tilde{D}_1 + \tilde{D}_2)\tilde{M}\pi^4 + 3\tilde{K}(6 + \sqrt{3}\tilde{M}\pi^2))^2} \Big) \Bigg)^{\frac{1}{2}}
\end{aligned} \tag{B.2}$$

•M – Γ:

$$\begin{aligned}
\max(\omega^-) =& \omega^-(\tilde{k}_1 = \pi, \tilde{k}_2 = \pi/\sqrt{3}) \\
=& \Bigg(\frac{1}{36\tilde{M}} \Big(18\tilde{K} + \tilde{M}\pi^2(3\sqrt{3}\tilde{K} + 18\pi^2 + 12\tilde{D}_1\pi^2 + 2\tilde{D}_2\pi^2) - \\
& \frac{3}{2}\sqrt{-64(9 + 6\tilde{D}_1 + \tilde{D}_2)\tilde{K}\tilde{M}\pi^4 + \frac{4}{9}(2(9 + 6\tilde{D}_1 + \tilde{D}_2)\tilde{M}\pi^4 + 3\tilde{K}(6 + \sqrt{3}\tilde{M}\pi^2))^2} \Big) \Bigg)^{\frac{1}{2}} \\
\min(\omega^+) =& \omega^+(k_1 = 0, k_2 = 0) = \sqrt{\left(\tilde{K}(3 + 2\sqrt{3}\tilde{M}) + \sqrt{3}\sqrt{\tilde{K}^2(3 + 4\tilde{M}(\sqrt{3} + \tilde{M}))} \right) / (6\tilde{M})}
\end{aligned} \tag{B.3}$$

where $\tilde{D}_1 = \tilde{D}_{12} + 2\tilde{D}_{66}$ and $\tilde{D}_2 = \tilde{D}_{22}$.

Appendix C. Direct asymptotic treatment and the floquet–bloch solution

The equations of motion for the orthotropic plate-resonator coupled system representing the honeycomb with the attached resonators are given by Eqs. (1). According to the method of multiple scales, the displacement of the plate $w(\mathbf{x})$ and the displacement z_{ij} of the jth resonator vibrating in its ith mode can be expressed in a power series of ε as:

$$w = \varepsilon w^{(1)}(x_0, y_0, x_2, y_2, T_0, T_2) + \varepsilon^3 w^{(3)}(x_0, y_0, x_2, y_2, T_0, T_2), \tag{C.1}$$

$$z_{ij} = \varepsilon z_{ij}^{(1)}(x_0, y_0, x_2, y_2, T_0, T_2) + \varepsilon^3 z_{ij}^{(3)}(x_0, y_0, x_2, y_2, T_0, T_2), \tag{C.2}$$

where we replaced the dependence on (x, y) with the fast space scales $(x_0, y_0) = (x, y)$ and slow scales $(x_2, y_2) = (\varepsilon^2 x, \varepsilon^2 y)$ and time t with the fast time scale $T_0 = t$ and the slow time scale $T_2 = \varepsilon^2 t$. By substituting Eqs. (C.1) and (C.2) into Eqs. (1) and equating terms of like powers of ε to zero, the following hierarchy of problems is obtained:

Order(ε) :

$$\rho^\star h D_0^2 w^{(1)} + \left[D_{11}^* \frac{\partial^4 w^{(1)}}{\partial x_0^4} + (2D_{12}^* + 4D_{66}^*) \frac{\partial^4 w^{(1)}}{\partial x_0^2 \partial y_0^2} + D_{22}^* \frac{\partial^4 w^{(1)}}{\partial y_0^4} \right] + \sum_{i,j} M_{ij} \left[D_0^2 w^{(1)} + D_0^2 z_{ij}^{(1)} \right] \delta(\mathbf{x}_0 - \mathbf{s}_j) = 0, \tag{C.3a}$$

$$M_{ij} \left[D_0^2 w^{(1)} + D_0^2 z_{ij}^{(1)} \right] + K_{ij} z_{ij}^{(1)} = 0, \tag{C.3b}$$

Order(ε^3) :

$$\rho^\star h D_0^2 w^{(3)} + \left[D_{11}^* \frac{\partial^4 w^{(3)}}{\partial x_0^4} + (2D_{12}^* + 4D_{66}^*) \frac{\partial^4 w^{(3)}}{\partial x_0^2 \partial y_0^2} + D_{22}^* \frac{\partial^4 w^{(3)}}{\partial y_0^4} \right] + \sum_{i,j} M_{ij} \left[D_0^2 w^{(3)} + D_0^2 z_{ij}^{(3)} \right] \delta(\mathbf{x}_0 - \mathbf{s}_j)$$
$$= -2\rho^\star h D_0 D_2 w^{(1)} - 2 \sum_{i,j} M_{ij} \left[D_0 D_2 w^{(1)} + D_0 D_2 z_{ij}^{(1)} \right] \delta(\mathbf{x}_0 - \mathbf{s}_j)$$
$$- 2 \left[D_{11}^* \frac{\partial^4 w^{(1)}}{\partial x_0^2 \partial x_2^2} + (2D_{12}^* + 4D_{66}^*) \left(\frac{\partial^4 w^{(1)}}{\partial x_0^2 \partial y_2^2} + \frac{\partial^4 w^{(1)}}{\partial x_2^2 \partial y_0^2} \right) + D_{22}^* \frac{\partial^4 w^{(1)}}{\partial y_0^2 \partial y_2^2} \right], \tag{C.3c}$$

$$M_{ij}(D_0^2 w^{(3)} + D_0^2 z_{ij}^{(3)}) + K_{ij} z_{ij}^{(3)} = -N_{ij}^{(3)} (z_{ij}^{(1)})^3 - 2M_{ij}(D_0 D_2 w^{(1)} + D_0 D_2 z_{ij}^{(1)}), \tag{C.3d}$$

where $\mathbf{s}_j = (x_{0j}, y_{0j})$ indicates the position vector of the jth resonator.

First order problem. The first order equations given by Eqs. ((C.3a), (C.3b)) are linear and represent the generating problem. One can here employ the Floquet–Bloch Theorem according to which the solution is sought as $w^{(1)}(x_0, y_0, T_0) = w_0^{(1)}(T_0) e^{i(k_1 x_0 + k_2 y_0)}$ and $z_{ij}^{(1)}(x_{0j}, y_{0j}, T_0) = z_{i0}^{(1)}(T_0) e^{i(k_1 x_{0j} + k_2 y_{0j})}$ where $w_0^{(1)}(T_0) = w^{(1)}(0, 0, T_0)$ and $z_{i0}^{(1)}(T_0) := z_{i0}^{(1)}(0, 0, T_0)$ denote the plate deflection and the relative resonator motion at the origin of the fixed frame. Upon substitution of the assumed solution into (1), one obtains

$$\left[\rho^\star h D_0^2 w_0^{(1)}(T_0) + [k_1^4 D_{11}^* + k_1^2 k_2^2 (2D_{12}^* + 4D_{66}^*) + k_2^4 D_{22}^*] w_0^{(1)}(T_0) \right] e^{i(k_1 x_0 + k_2 y_0)} + \sum_{i,j} M_{ij} \left[D_0^2 w_0^{(1)}(T_0) + D_0^2 z_{i0}^{(1)}(T_0) \right] e^{i(k_1 x_0 + k_2 y_0)} \delta(x_0 - x_{0j}) \delta(y_0 - y_{0j}) = 0, \tag{C.4a}$$

$$M_{ij} \left[D_0^2 w_0^{(1)}(T_0) + D_0^2 z_{i0}^{(1)}(T_0) \right] + K_{ij} z_{i0}^{(1)}(T_0) = 0. \tag{C.4b}$$

Given the periodicity of the solution, the plate equation of motion is projected onto the unit cell domain Ω_x (i.e., the lattice unit is periodically repeated along the lattice vector directions) to yield

$$\int_{\Omega_x} \left[\rho^\star h D_0^2 w_0^{(1)}(T_0) + (k_1^4 D_{11}^* + k_1^2 k_2^2 (2D_{12}^* + 4D_{66}^*) + k_2^4 D_{22}^*) w_0^{(1)}(T_0) \right] e^{i(k_1 x_0 + k_2 y_0)} dx_0 dy_0 + \int_{\Omega_x} \left\{ \sum_{ij} M_{ij} \left[D_0^2 w_0^{(1)}(T_0) + D_0^2 z_{i0}^{(1)}(T_0) \right] e^{i(k_1 x_0 + k_2 y_0)} \delta(x_0 - x_j) \delta(y_0 - y_j) \right\} dx_0 dy_0 = 0, \tag{C.5}$$
$$M_{ij} \left[D_0^2 w_0^{(1)}(T_0) + D_0^2 z_{i0}^{(1)}(T_0) \right] + K_{ij} z_{i0}^{(1)}(T_0) = 0.$$

For the metamaterial lattice with an array of equally spaced single-dof resonators (so that the subscripts in M_{ij}, K_{ij} can be dropped), the first order equations read:

$$\begin{bmatrix} M_H(k_1, k_2) + M & M \\ M & M \end{bmatrix} \begin{bmatrix} D_0^2 w_0^{(1)} \\ D_0^2 z_0^{(1)} \end{bmatrix} + \begin{bmatrix} K_H(k_1, k_2) & 0 \\ 0 & K \end{bmatrix} \begin{bmatrix} w_0^{(1)} \\ z_0^{(1)} \end{bmatrix} = \begin{bmatrix} 0 \\ 0 \end{bmatrix}. \tag{C.6}$$

Upon searching for solutions of the form $[w_0^{(1)}, z_0^{(1)}] = A(x_2, y_2, T_2) \boldsymbol{\phi} \exp(i\omega T_0)$, the ensuing eigenvalue problem is expressed as:

$$(\mathbf{K} - \omega^2 \mathbf{M}) \boldsymbol{\phi} = \mathbf{0}, \tag{C.7}$$

where the column vector $\boldsymbol{\phi}$ denotes the eigenvector and the mass and stiffness matrices are given by

$$\mathbf{M} = \begin{bmatrix} M_H(k_1, k_2) + M & M \\ M & M \end{bmatrix} \quad \text{and} \quad \mathbf{K} = \begin{bmatrix} K_H(k_1, k_2) & 0 \\ 0 & K \end{bmatrix}. \tag{C.8}$$

where

$$K_H = A_k(k_1, k_2) \left[k_1^4 + k_1^2 k_2^2 2(D_{12}^* + 2D_{66}^*) + k_2^4 D_{22}^* \right] \tag{C.9}$$

and $M_H = \rho^* h A_k(k_1, k_2)$ with

$$A_k(k_1,k_2) = \frac{4\sqrt{3}\sin\left(\frac{k_1}{2}\right)\sin\left(\frac{1}{4}\left(k_1+\sqrt{3}k_2\right)\right)}{k_1\left(k_1+\sqrt{3}k_2\right)}. \tag{C.10}$$

Setting the determinant of the coefficient matrix in Eq. (C.7) to zero yields the linear dispersion equation:

$$\det(\mathbf{K}-\omega^2\mathbf{M}) = 0, \tag{C.11}$$

whose roots denoted by ω^- and ω^+ are the frequencies of the acoustic mode $\boldsymbol{\phi}^-$ and the optical mode $\boldsymbol{\phi}^+$, respectively.

The first order solutions of the plate displacement and the resonator motion at the origin are expressed as

$$w_0^{(1)} = A^{\pm}(x_2,y_2,T_2)\phi_1^{\pm}e^{(i\omega^{\pm}T_0)} + c.c. \tag{C.12}$$

$$z_0^{(1)} = A^{\pm}(x_2,y_2,T_2)\phi_2^{\pm}e^{(i\omega^{\pm}T_0)} + c.c. \tag{C.13}$$

where $A^{\pm}(x_2,y_2,T_2)$ is the slowly-varying (in space and time) complex-valued amplitude. We take + or- depending on whether the acoustic or the optical wave is sought to be expanded. The cubic resonator restoring force $[z_0^{(1)}]^3$ will generate terms proportional to $(A^{\pm})^2\bar{A}^{\pm}(\phi_2^{\pm})^3e^{i\omega^{\pm}T_0}$ (i.e., $\bar{A}^{\pm}$ is the complex conjugate of $A^{\pm}$) which induce resonance effects on either the acoustic or the optical mode. For a more general treatment as discussed in Section 4, we assume that the first-order solution contains both the acoustic and optical wave eigenvectors; that is,

$$w_0^{(1)} = A^-(x_2,y_2,T_2)\phi_1^-e^{i\omega^-T_0} + A^+(x_2,y_2,T_2)\phi_1^+e^{i\omega^+T_0} + c.c. \tag{C.14}$$

$$z_0^{(1)} = A^-(x_2,y_2,T_2)\phi_2^-e^{i\omega^-T_0} + A^+(x_2,y_2,T_2)\phi_2^+e^{i\omega^+T_0} + c.c. \tag{C.15}$$

This approach will generate resonance terms proportional to $(A^-)^2\bar{A}^-(\phi_2^-)^3e^{i\omega^-T_0}$ and

$A^-A^+\bar{A}^+\phi_2^-(\phi_2^+)^2e^{i\omega^-T_0}$ for the acoustic mode or $(A^+)^2\bar{A}^+(\phi_2^+)^3e^{i\omega^+T_0}$ and $A^+A^-\bar{A}^-\phi_2^+(\phi_2^-)^2e^{i\omega^+T_0}$ for the optical mode. Thus, the first order solution $w^{(1)}$ and $z_{ij}^{(1)}$ is expressed as

$$\begin{aligned} w^{(1)} &= A^+(T_2,x_2,y_2)\phi_1^+e^{i\omega^+T_0}e^{i(k_1x_0+k_2y_0)} + A^-(T_2,x_2,y_2)\phi_1^-e^{i\omega^-T_0}e^{i(k_1x_0+k_2y_0)} + c.c.,\\ z_{ij}^{(1)} &= A^+(T_2,x_2,y_2)\phi_2^+e^{i\omega^+T_0}e^{i(k_1x_{0j}+k_2y_{0j})} + A^-(T_2,x_2,y_2)\phi_2^-e^{i\omega^-T_0}e^{i(k_1x_{0j}+k_2y_{0j})} + c.c.. \end{aligned} \tag{C.16}$$

Third order problem. Substituting the first order solution (C.16) into the right-hand side of Eqs. ((C.3c), (C.3d)) yields the cubic problem:

$$\begin{aligned} &\rho^\star h D_0^2 w^{(3)} + \left[D_{11}^*\frac{\partial^4 w^{(3)}}{\partial x_0^4} + (2D_{12}^*+4D_{66}^*)\frac{\partial^4 w^{(3)}}{\partial x_0^2\partial y_0^2} + D_{22}^*\frac{\partial^4 w^{(3)}}{\partial y_0^4}\right] \\ &\quad + \sum_{i,j} M_{ij}\left[D_0^2 w^{(3)} + D_0^2 z_{ij}^{(3)}\right]\delta(\mathbf{x}_0-\mathbf{s}_j) = \Big\{ -2i\omega^{\pm}\rho^\star h\phi_1^{\pm}D_2A^{\pm} \\ &\quad - 2\sum_{i,j} i\omega^{\pm}M_{ij}(\phi_1^{\pm}+\phi_2^{\pm})D_2A^{\pm}\delta(\mathbf{x_0}-\mathbf{s}_j) - 2\phi_1^{\pm}\Big[D_{11}^*\frac{\partial^4 A^{\pm}}{\partial x_0^2\partial x_2^2} \\ &\quad + (2D_{12}^*+4D_{66}^*)\Big(\frac{\partial^4 A^{\pm}}{\partial x_0^2\partial y_2^2} + \frac{\partial^4 A^{\pm}}{\partial x_2^2\partial y_0^2}\Big) + D_{22}^*\frac{\partial^4 A^{\pm}}{\partial y_0^2\partial y_2^2}\Big]\Big\} e^{i\omega^{\pm}T_0}e^{i(k_1x_0+k_2y_0)} + c.c., \end{aligned} \tag{C.17a}$$

$$\begin{aligned} &M_{ij}\left[D_0^2 w^{(3)}(x_2,y_2,T_2) + D_0^2 z_{ij}^{(3)}(x_2,y_2,T_2)\right] + K_{ij}z_{ij}^{(3)}(x_2,y_2,T_2) \\ &\quad = \Big[-2i\omega^{\pm}M_{ij}(\phi_1^{\pm}+\phi_2^{\pm})D_2A^{\pm} \\ &\quad - 3N_{ij}^{(3)}((A^{\pm})^2\bar{A}^{\pm}(\phi_2^{\pm})^3 + 2A^{\pm}A^{\mp}\bar{A}^{\mp}\phi_2^{\pm}(\phi_2^{\mp})^2)\Big]e^{i\omega^{\pm}T_0}e^{i(k_1x_{0j}+k_2y_{0j})} + NST + c.c., \end{aligned} \tag{C.17b}$$

where *NST* represents terms that do not cause secular effects due to the cubic nonlinearity. Given the periodic nature of the resonance forcing terms, the periodicity is enforced again according to $w^{(3)} = w_0^{(3)}e^{i(k_1x_0+k_2y_0)}$ and $z_{ij}^{(3)} = z_0^{(3)}e^{i(k_1x_{0j}+k_2y_{0j})}$ (for the case of one resonator per unit cell). The ensuing third order equation (C.17a) is projected onto the unit cell domain Ω_x, after carrying out the nondimensionalization procedure expressed by Eq. (11). The reduced equations become

$$\begin{aligned} &\tilde{M}_H D_0^2\tilde{w}_0^{(3)} + \tilde{K}_H\tilde{w}_0^{(3)} + \tilde{M}\left[D_0^2\tilde{w}_0^{(3)} + D_0^2\tilde{z}_0^{(3)}\right] = \Big\{ -2i\omega^{\pm}\tilde{M}_H\phi_1^{\pm}D_2A^{\pm} \\ &\quad - 2i\omega^{\pm}\tilde{M}(\phi_1^{\pm}+\phi_2^{\pm})D_2A^{\pm} + 2\tilde{A}(\tilde{k}_1,\tilde{k}_2)\phi_1^{\pm}\Big[\tilde{D}_{11}\frac{\tilde{k}_1^2\partial^2 A^{\pm}}{\partial\tilde{x}_2^2} \\ &\quad + (2\tilde{D}_{12}+4\tilde{D}_{66})\Big(\frac{\tilde{k}_1^2\partial^2 A^{\pm}}{\partial\tilde{y}_2^2} + \frac{\tilde{k}_2^2\partial^2 A^{\pm}}{\partial\tilde{x}_2^2}\Big) + \tilde{D}_{22}\frac{\tilde{k}_2^2\partial^2 A^{\pm}}{\partial\tilde{y}_2^2}\Big]\Big\} e^{i\omega^{\pm}T_0} + c.c., \end{aligned} \tag{C.18a}$$

$$\tilde{M}(D_0^2\tilde{w}_0^{(3)} + D_0^2\tilde{z}_0^{(3)}) + \tilde{K}\tilde{z}_0^{(3)} = \Big[-2i\omega^{\pm}\tilde{M}(\phi_1^{\pm} + \phi_2^{\pm})D_2A^{\pm} - 3\tilde{N}^{(3)}\left((A^{\pm})^2\bar{A}^{\pm}(\phi_2^{\pm})^3 + 2A^{\pm}A^{\mp}\bar{A}^{\mp}\phi_2^{\pm}(\phi_2^{\mp})^2 \right)\Big] e^{i\omega^{\pm}T_0} + NST + c.c.. \tag{C.18b}$$

By enforcing the solvability condition in equations (C.18a) and (C.18b), one renders the inhomogeneous terms orthogonal to the solution of the adjoint problem, $[\tilde{w}_0^*, \tilde{z}_0^*]^{\top} = [\phi_1^{\pm}, \phi_2^{\pm}]e^{-i\omega^{\pm}T_0}$, to obtain

$$\begin{aligned}
&\phi_1^{\pm}\Big\{ -2i\omega^{\pm}\tilde{M}_H\phi_1^{\pm}D_2A^{\pm} - 2i\tilde{M}\omega^{\pm}(\phi_1^{\pm} + \phi_2^{\pm})D_2A^{\pm} + 2\tilde{A}(\tilde{k}_1, \tilde{k}_2)\phi_1^{\pm}(\tilde{D}_{11}\frac{\tilde{k}_1^2\partial^2A^{\pm}}{\partial\tilde{x}_2^2} \\
&+ (2\tilde{D}_{12} + 4\tilde{D}_{66})(\frac{\tilde{k}_1^2\partial^2A^{\pm}}{\partial\tilde{y}_2^2} + \frac{\tilde{k}_2^2\partial^2A^{\pm}}{\partial\tilde{x}_2^2}) + \tilde{D}_{22}\frac{\tilde{k}_2^2\partial^2A^{\pm}}{\partial\tilde{y}_2^2}) \Big\} \\
&+ \phi_2^{\pm}\Big\{ -2i\omega^{\pm}\tilde{M}(\phi_2^{\pm} + \phi_1^{\pm})D_2A^{\pm} - 3\tilde{N}^{(3)}\left((\phi_2^{\pm})^3(A^{\pm})^2\bar{A}^{\pm} + 2A^{\pm}A^{\mp}\bar{A}^{\mp}\phi_2^{\pm}(\phi_2^{\mp})^2 \right)\Big\} = 0.
\end{aligned} \tag{C.19}$$

Setting the slow space derivative terms to zero (i.e., the nonlinear frequency modulation of the waves is sought) yields the modulation equation as

$$\begin{aligned}
&-2i\omega^{\pm}[\tilde{M}_H(\phi_1^{\pm})^2 + \tilde{M}((\phi_1^{\pm})^2 + (\phi_2^{\pm})^2 + 2\phi_1^{\pm}\phi_2^{\pm})]D_2A^{\pm} \\
&\quad - 3\tilde{N}^{(3)}\left[(\phi_2^{\pm})^4(A^{\pm})^2\bar{A}^{\pm} + 2A^{\pm}A^{\mp}\bar{A}^{\mp}(\phi_2^{\pm})^2(\phi_2^{\mp})^2 \right] = 0,
\end{aligned} \tag{C.20}$$

By taking into account in Eq. (C.20) of the eigenvector normalization condition

$$(\tilde{M}_H + \tilde{M})(\phi_1^{\pm})^2 + 2\tilde{M}\phi_2^{\pm}\phi_1^{\pm} + \tilde{M}(\phi_2^{\pm})^2 = 1, \tag{C.21}$$

one obtains the final modulation equation as

$$2i\omega^{\pm}D_2A^{\pm} + 3\tilde{N}^{(3)}\left[(\phi_2^{\pm})^4(A^{\pm})^2\bar{A}^{\pm} + 2A^{\pm}A^{\mp}\bar{A}^{\mp}(\phi_2^{\pm})^2(\phi_2^{\mp})^2\right] = 0. \tag{C.22}$$

The equations obtained here by direct asymptotic treatment are exactly the same as Eq. (29).

References

[1] G.U. Patil, K.H. Matlack, Review of exploiting nonlinearity in phononic materials to enable nonlinear wave responses, Acta Mech. (2021) 1–46.
[2] L. Van Belle, C. Claeys, E. Deckers, W. Desmet, Implications of nonsub-wavelength resonator spacing on the sound transmission loss predictions of locally resonant metamaterial partitions, J. Vib. Acoust. 143 (4) (2021) 044503.
[3] X. Fang, K.-C. Chuang, X.-L. Jin, D.-F. Wang, Z.-L. Huang, An inertant elastic metamaterial plate with extra wide low-frequency flexural band gaps, J. Appl. Mech. 88 (2) (2021) 021002.
[4] Y. Xue, J. Li, Y. Wang, F. Li, Tunable nonlinear band gaps in a sandwich-like meta-plate, Nonlinear Dynam. 106 (2021) 2841–2857.
[5] H. Danawe, S. Tol, Experimental realization of negative refraction and subwavelength imaging for flexural waves in phononic crystal plates, J. Sound Vib. 518 (2022) 116552.
[6] A. Foehr, O.R. Bilal, S.D. Huber, C. Daraio, Spiral-based phononic plates: From wave beaming to topological insulators, Phys. Rev. Lett. 120 (20) (2018) 205501.
[7] V.F. Dal Poggetto, A.L. Serpa, Flexural wave band gaps in a ternary periodic metamaterial plate using the plane wave expansion method, J. Sound Vib. 495 (2021) 115909.
[8] L. Liu, A. Sridhar, M. Geers, V. Kouznetsova, Computational homogenization of locally resonant acoustic metamaterial panels towards enriched continuum beam/shell structures, Comput. Methods Appl. Mech. Engrg. 387 (2021) 114161.
[9] L. Fan, Y. He, X.-a. Chen, X. Zhao, A frequency response function-based optimization for metamaterial beams considering both location and mass distributions of local resonators, J. Appl. Phys. 130 (11) (2021) 115101.
[10] J. Jung, S. Goo, S. Wang, Investigation of flexural wave band gaps in a locally resonant metamaterial with plate-like resonators, Wave Motion 93 (2020) 102492.
[11] C. Lim, J.T. Li, Z. Zhao, et al., Lightweight architected lattice phononic crystals with broadband and multiband vibration mitigation characteristics, Extreme Mech. Lett. 41 (2020) 100994.
[12] R. Chaunsali, C.-W. Chen, J. Yang, Subwavelength and directional control of flexural waves in zone-folding induced topological plates, Phys. Rev. B 97 (5) (2018) 054307.
[13] E. Miranda Jr., S. Rodrigues, C. Aranas Jr., J. Dos Santos, Plane wave expansion and extended plane wave expansion formulations for Mindlin–Reissner elastic metamaterial thick plates, J. Math. Anal. Appl. 505 (2) (2022) 125503.
[14] W. Guo, Z. Yang, Q. Feng, C. Dai, J. Yang, X. Lei, A new method for band gap analysis of periodic structures using virtual spring model and energy functional variational principle, Mech. Syst. Signal Process. 168 (2022) 108634.
[15] A. Bacigalupo, L. Gambarotta, Simplified modelling of chiral lattice materials with local resonators, Int. J. Solids Struct. 83 (2016) 126–141.
[16] C. Comi, L. Driemeier, Wave propagation in cellular locally resonant metamaterials, Lat. Am. J. Solids Struct. 15 (2018).
[17] K.H. Matlack, A. Bauhofer, S. Krödel, A. Palermo, C. Daraio, Composite 3D-printed metastructures for low-frequency and broadband vibration absorption, Proc. Natl. Acad. Sci. 113 (30) (2016) 8386–8390.
[18] E. Miranda Jr., E. Nobrega, S. Rodrigues, C. Aranas Jr., J. Dos Santos, Wave attenuation in elastic metamaterial thick plates: Analytical, numerical and experimental investigations, Int. J. Solids Struct. 204 (2020) 138–152.
[19] Q. Wang, J. Li, Y. Zhang, Y. Xue, F. Li, Bandgap properties in metamaterial sandwich plate with periodically embedded plate-type resonators, Mech. Syst. Signal Process. 151 (2021) 107375.
[20] C. Cai, J. Zhou, K. Wang, H. Pan, D. Tan, D. Xu, G. Wen, Flexural wave attenuation by metamaterial beam with compliant quasi-zero-stiffness resonators, Mech. Syst. Signal Process. 174 (2022) 109119.
[21] G.L. Holst, G.H. Teichert, B.D. Jensen, Modeling and experiments of buckling modes and deflection of fixed-guided beams in compliant mechanisms, J. Mech. Des. 133 (5) (2011).
[22] Y.-H. Chen, C.-C. Lan, An adjustable constant-force mechanism for adaptive end-effector operations, J. Mech. Des. 134 (3) (2012).

[23] C.-W. Hou, C.-C. Lan, Functional joint mechanisms with constant-torque outputs, Mech. Mach. Theory 62 (2013) 166–181.
[24] J.R. Raney, N. Nadkarni, C. Daraio, D.M. Kochmann, J.A. Lewis, K. Bertoldi, Stable propagation of mechanical signals in soft media using stored elastic energy, Proc. Natl. Acad. Sci. 113 (35) (2016) 9722–9727.
[25] C. Lim, Z. Yaw, Z. Chen, et al., Periodic and aperiodic 3-D composite metastructures with ultrawide bandgap for vibration and noise control, Compos. Struct. 287 (2022) 115324.
[26] Z. Liu, X. Zhang, Y. Mao, Y.Y. Zhu, Z. Yang, C.T. Chan, P. Sheng, Locally resonant sonic materials, Science 289 (5485) (2000) 1734–1736.
[27] A. Casalotti, S. El-Borgi, W. Lacarbonara, Metamaterial beam with embedded nonlinear vibration absorbers, Int. J. Non-Linear Mech. 98 (2018) 32–42.
[28] Y. Shen, W. Lacarbonara, Nonlinear dispersion properties of metamaterial beams hosting nonlinear resonators and stop band optimization, Mech. Syst. Signal Process. 187 (2023) 109920.
[29] A. Fortunati, A. Bacigalupo, M. Lepidi, A. Arena, W. Lacarbonara, Nonlinear wave propagation in locally dissipative metamaterials via Hamiltonian perturbation approach, Nonlinear Dynam. 108 (2) (2022) 765–787.
[30] Y. Xiao, J. Wen, X. Wen, Flexural wave band gaps in locally resonant thin plates with periodically attached spring–mass resonators, J. Phys. D: Appl. Phys. 45 (19) (2012) 195401.
[31] E. Miranda Jr., J. Dos Santos, Flexural wave band gaps in elastic metamaterial thin plate, in: Proceedings of the IX Mechanical Engineering Brazilian Congress, 2016, pp. 1–10.
[32] Q. Qin, M.-P. Sheng, Analyses of multi-bandgap property of a locally resonant plate composed of periodic resonant subsystems, Internat. J. Modern Phys. B 32 (24) (2018) 1850269.
[33] Q. Li, M. Sheng, An improved method for bandgap calculation of a locally resonant plate with multi-periodic of multiple degree-of-freedom resonators, J. Appl. Phys. 129 (24) (2021) 245110.
[34] A.H. Nayfeh, D.T. Mook, Nonlinear Oscillations, John Wiley & sons, New-York, 1979.
[35] R.K. Narisetti, M.J. Leamy, M. Ruzzene, A perturbation approach for predicting wave propagation in one-dimensional nonlinear periodic structures, J. Vib. Acoust. 132 (2010) 031001–11.
[36] M.D. Fronk, M.J. Leamy, Direction-dependent invariant waveforms and stability in two-dimensional, weakly nonlinear lattices, J. Sound Vib. 447 (2019) 137–154.
[37] M. Bukhari, O. Barry, Spectro-spatial analyses of a nonlinear metamaterial with multiple nonlinear local resonators, Nonlinear Dynam. 99 (2020) 1539–1560.
[38] M. Lepidi, A. Bacigalupo, Wave propagation properties of one-dimensional acoustic metamaterials with nonlinear diatomic microstructure, Nonlinear Dynam. 98 (2019) 2711–2735.
[39] M.D. Fronk, M.J. Leamy, Internally resonant wave energy exchange in weakly nonlinear lattices and metamaterials, Phys. Rev. E 100 (2019) 032213.
[40] K. Manktelow, M.J. Leamy, M. Ruzzene, Multiple scales analysis of wave-wave interactions in a cubically nonlinear monoatomic chain, Nonlinear Dynam. 63 (2011) 193–203.
[41] M.D. Fronk, M.J. Leamy, Higher-order dispersion, stability, and waveform invariance in nonlinear monoatomic and diatomic systems, J. Vib. Acoust. 139 (2017) 051003–13.
[42] L. Fang, M.J. Leamy, Perturbation analysis of nonlinear evanescent waves in a one-dimensional monatomic chain, Phys. Rev. E 105 (2022) 014203.
[43] L.J. Gibson, M.F. Ashby, Cellular Solids: Structure and Properties, second ed., in: Cambridge Solid State Science Series, Cambridge University Press, 1997, http://dx.doi.org/10.1017/CBO9781139878326.
[44] S. Malek, L. Gibson, Effective elastic properties of periodic hexagonal honeycombs, Mech. Mater. 91 (2015) 226–240.
[45] S. Sorohan, D.M. Constantinescu, M. Sandu, A.G. Sandu, On the homogenization of hexagonal honeycombs under axial and shear loading. Part I: Analytical formulation for free skin effect, Mech. Mater. 119 (2018) 74–91.
[46] M. Murer, S. Guruva, G. Formica, W. Lacarbonara, A multi-bandgap metamaterial with multi-frequency resonators, J. Compos. Mater. (2023) 1–22.
[47] W. Lacarbonara, Nonlinear Structural Mechanics. Theory, Dynamical Phenomena and Modeling, first ed., Springer, 2013.
[48] W. Lacarbonara, R. Camillacci, Nonlinear normal modes of structural systems via asymptotic approach, Int. J. Solids Struct. 41 (2004) 5565–5594.
[49] V. Settimi, M. Lepidi, A. Bacigalupo, Nonlinear dispersion properties of one-dimensional mechanical metamaterials with inertia amplification, Int. J. Mech. Sci. 201 (2021) 106461.